Theoretical Considerations for Experiments to Create and Detect Localised Majorana Modes in Electronic Systems

Theoretical Considerations for Experiments to Create and Detect Localised Majorana Modes in Electronic Systems

A thesis presented

by

Gilad Ben-Shach

to

The Department of Physics

in partial fulfillment of the requirements

for the degree of

Doctor of Philosophy

in the subject of

Physics

Harvard University

Cambridge, Massachusetts

December 2014

Thesis advisor

Bertrand I. Halperin and Amir Yacoby

Author

Gilad Ben-Shach

Theoretical Considerations for Experiments to Create and Detect Localised Majorana Modes in Electronic Systems

Abstract

This thesis presents our work on building a bridge between the theoretical proposals for the condensed matter realisation of peculiar localised excitations, known as Majorana modes, and experiments to search for them. The main focus in the first two sections is on charge sensing of localised Majorana modes in two distinct systems. First, we address the properties of charged quasiparticles in the $\nu = 5/2$ fractional quantum Hall regime. In particular, we focus on the case where these particles are trapped by disorder, often in close proximity to one another. Next, we consider one-dimensional semi-conducting wires with strong spin-orbit coupling and proximity-induced superconductivity. The Majorana modes in this system are predicted to be charge-neutral. We show, however, that when the wire is short enough, there is a uniform charge distribution along the wire, and we show how the presence of this charge depends on system parameters. A third portion is related to HgTe quantum wells, another system predicted to host Majorana modes when coupled to a superconductor. Here we consider a HgTe well in the metallic regime, coupled to two superconducting strips. We compute the Josephson coupling in the presence of spin-orbit interactions and in-plane external magnetic fields.

Contents

Title Page i
Abstract iii
Table of Contents iv
Citations to previously published work vi
Acknowledgments vii
Dedication x

1 Introduction **1**
1.1 Overview 1
1.2 Organization of the dissertation 4
1.3 Topological Physics 5
1.4 Anyons 6
1.5 Non-Abelian Anyons 7
1.5.1 The Braid Group 7
1.5.2 Non-Abelian Braiding Statistics 9
1.5.3 Fusion 9
1.6 Topological Quantum Computers 11
1.7 $\nu = 5/2$ FQHE 12
1.7.1 Electrons in 2D & Magnetic Fields 13
1.7.2 Interactions and Fractions - 5/2 14
1.7.3 Fractional Charge and SETs 16
1.8 1D wires 17
1.8.1 Bogoliubov de Gennes 18
1.9 HgTe 20
1.9.1 Topological Insulators 20
1.9.2 Induced Superconductivity 21
1.10 Real Systems 21

2 Detecting Non-Abelian Anyons by Charging Spectroscopy **24**
2.1 Overview 24
2.2 Introduction 25

2.3 Qualitative Picture . . . 27
2.4 Equilibration . . . 30
2.5 Quantitative Picture . . . 31
2.6 One Particle . . . 32
2.7 Two Particles . . . 33
2.8 Circular Well . . . 34
2.9 Anisotropic Well . . . 36
2.10 Energy Estimates . . . 37
2.11 Matrix Elements . . . 38
2.12 Saddle Point . . . 39
2.13 2-particle Splittings . . . 40
2.14 Relations between κ , the local incompressibility, and the SET signal. 43
2.14.1 Chemical Potential v. Backgate . . . 43
2.14.2 Relation of the SET signal to the local incompressibility . . . 43
2.14.3 Relation between the SET signal and the local quasiparticle compressibility . . . 45
2.14.4 Calculation of $\eta(d)$ . . . 47
2.15 Conclusion . . . 48

3 Detecting Majoranas in 1D wires by charge sensing 49
3.1 Overview . . . 49
3.2 Introduction . . . 50
3.3 Modeling . . . 56
3.4 Spectrum and Parity . . . 57
3.5 Jumps in charge density . . . 65
3.6 Numerical Calculations of Total Charge . . . 70
3.7 Numerical Calculations of the Charge Distribution . . . 73
3.8 Jumps in Spin Density . . . 75
3.9 Effects of Electron-Electron Interactions . . . 76
3.10 Experiment . . . 80
3.11 Methods for Calculating Number Parity . . . 82
3.12 Conclusion . . . 85

4 Induced Superconductivity and Spin-Orbit Coupling 86
4.1 Motivation - HgTe . . . 86
4.2 Model . . . 87
4.3 Scattering . . . 88
4.4 Results . . . 97

Bibliography 100

Citations to previously published work

Parts of this dissertation cover research reported in the following articles:

1. "Detecting Non-Abelian Anyons by Charging Spectroscopy," G. Ben-Shach, C.R. Laumann, I. Neder, A. Yacoby, and B.I. Halperin. *Phys. Rev. Lett.* **110**, 106805 (2013)

2. "Detecting Majorana modes in one-dimensional wires by charge sensing," G. Ben-Shach, A. Haim, I. Appelbaum, Y. Oreg, A. Yacoby, B.I. Halperin. *Phys. Rev. B* **91**, 045403 (2015)

Acknowledgments

Some students have an advisor who is a brilliant scientist. Others have an advisor who is a great person. The lucky student has an advisor who is both. Somehow, I ended up with *two* advisors, both of whom are awe-inspiring physicists and amazing people. This thesis marks the end of five and a half great years at Harvard, and would not have been possible without them.

Bert Halperin's intuition is second to none. Not only does he have a deep understanding of the big-picture of any and every physical system you throw at him, he has a magical ability to pull factors of 2π out of thin-air, and is always correct. I once heard somebody say that Bert is never wrong about physics, and all the evidence I have seen supports that claim. Bert's knowledge extends far beyond science, which makes every lunch conversation a unique experience. I even had the privilege of a Bert-lead private tour of the art at the Harvard law school, after I questioned whether or not a statue was "actually art".

Amir Yacoby's ability to look at what most people would call noise and see an experimental signal is mind-boggling. His vision and passion are incredible. Whether discussing physics or other topics, chatting with Amir over coffee or a run would always leave me newly invigorated. I also want to take this opportunity to thank the whole Yacoby group for welcoming a lonely theorist into the lab.

Guillaume Gervais, Uzy Smilansky, and the late Bob Moore provided me with incredible research opportunities before coming to Harvard. Rami Band gave me the confidence and guidance to do independent research. Chris Laumann, Izhar Neder, Jay Sau, Anton Akhmerov, Johannes Bauer and Mark Rudner were all very patient teachers as I got acquainted with my new field. Sean Hart, Vivek Ventakachalam and

Hechen Ren shared and explained their beautiful data to me, much of which inspired the work discussed in this thesis. Thank you to Gilad Barak, Chris Laumann, and Ilya Feige for helping me develop my programming skills.

Part of the research on one-dimensional wires was done at the University of Copenhagen, and I thank Karsten Flensberg and Charlie Marcus for their hospitality. The wire paper was done in collaboration with people at Weizmann, and I thank Yuval Oreg for generously hosting me in Israel on several visits, and for his valuable guidance throughout the project. It was a pleasure to collaborate with Arbel Haim and Ian Appelbaum. I would also like to thank Eugene Demler for being on my PhD committee.

Carolyn Moore, Jen Bastin, Lisa Cacciabaudo and Sheila Ferguson are amazingly good at their jobs and made sure all logistical details of the PhD were taken care of quickly and efficiently. The physics department and Misha Lukin get a special thank you for helping make physics hockey a reality. Also thank you to the Harvard Fencing Team for welcoming me to their ranks.

My parents have always been my greatest supporters. I would not have been able to start, or finish, this PhD without their amazing dedication and devotion. Nitai, my brother and best friend, always reminded me that I am a "mathlete and not an athlete," which kept me focused on school when I was dreaming of the Olympics. My grandparents are a never-ending source of encouragement, and their requests for constant updates on my progress kept me in line and helped me finish this PhD on schedule. My in-laws, although added late in the PhD, have quickly joined the pack of wonderful family supporters.

And finally, there is my sneaky little Russian wife – Bella. From surprising me with celebratory dessert whenever I completed a task, to coaching me for my lectures, Bella has been by my side since we met. She always knows how to make sure I disengage from my work, and often seems to know me better than I know myself. I could not have asked for a better person to share this experience with. Although this thesis marks my transition to a new stage in life, I am comforted to know that Bella's presence remains a constant.

Acknowledgements of Financial Support

This thesis is based on work funded by NSERC, FQRNT, NSF, Microsoft Corporation, and STC Centre for Integrated Quantum Materials.

To Ingie, for getting me out of bed every morning.

Chapter 1

Introduction

1.1 Overview

This thesis presents our work on building a bridge between the theoretical proposals for the condensed matter realisation of peculiar localised excitations, known as Majorana modes, and experiments to search for them. These excitations have been predicted to occur in certain "topological states" of many-electron systems. In the limit where the Majorana locations are far apart, they create modes of very low energy inside a bulk energy gap. In particular, the overarching theme of the research presented is the detection of these modes, predicted to exist in various topological states of matter, through charge sensing measurements. Should these topological states really host the isolated Majorana modes as predicted, there is hope that they can be used to construct a topological, fault-tolerant, quantum computer. The energy splitting between several modes in a system is exponentially small in the distance between particles when they are well separated. This allows for manipulations that give

rise to definite unitary transformations within the low energy Hilbert space, provided that they are done on a time scale fast compared to the inverse energy splitting.

Although the existence of Majorana modes is well established in theoretical models, the experimental search is non-trivial. This search is underway, and although some results are intriguing, there is still a lack of conclusive evidence. This thesis is concerned with the search for evidence of these states in three rather different systems.

As mentioned above, several Majorana modes in a system interact with each other at finite distances and their degeneracies are split by these interactions. Whereas other theoretical works often focus on the non-interacting limit, we exploit these interactions here to predict new experimental signatures. We make these predictions in both two-dimensional and one-dimensional systems. The main ingredients – mid-gap (nearly) degenerate states and charge sensing – are common to both systems. However, the physics – and hence the meaning of the charge that we sense – is actually quite different in the two cases. In a separate chapter of the thesis, we address a more recent arrival to the jungle of topological systems under consideration, namely HgTe quantum wells.

The first system we consider is the $\nu = 5/2$ fractional quantum Hall state. This state occurs in very clean two-dimensional systems in the presence of a strong magnetic field. It has been directly observed in GaAs quantum wells, as a plateau in the Hall conductance. The elementary excitations in this state are predicted to have charge $e/4$, with Majorana modes attached to these excitations. If these charges are localised and far apart, the Majorana modes contribute an entropy to the system. Various schemes exist to experimentally look for this entropy. We are concerned with

an attempt to see the effects of this entropy on the charging spectrum of the system. Specifically, we examine how charge can enter a region under a scanning tip sensor as the potential on a global back-gate is varied. We predict the behaviour of individual charging events as a result of this entropy at very low but finite temperatures. The theory is complicated by the fact that the quasiparticles can be trapped by local disorder, but they move around within the wells in which they sit.

Another system we consider consists of a semi-conducting nanowire with strong spin-orbit coupling, with an external magnetic field and proximity-induced superconductivity. Such a system is predicted to host Majorana modes at the ends of the wire under the right conditions. There have been promising experimental efforts made on these wires, but debate still exists as to the interpretation of the results. We propose a new experiment to sense small changes in the electric charge in the nanowire, as we vary a global external gate or the applied magnetic field, in wires short enough that the wavefunctions of the Majorana modes overlap. Among other results, we predict that the charge associated with the Majorana states at the ends is actually uniformly distributed along the wire's length.

Finally, we discuss proximity induced superconductivity in HgTe quantum wells. HgTe wells are exciting because they can be put in a topological insulating state which is a quantum spin Hall conductor. When in this topological insulator state, there is a one-dimensional metal at the edge, and if properly coupled to a superconductor, the edge can exhibit Majorana modes. The experiments we are interested in are not yet looking for Majorana modes, but understanding how superconductors couple to the material, and in particular, we do not focus on the insulating state. Superconductivity

is a requirement to eventually see Majorana modes, and it is therefore marginally related to the other chapters. In particular, we examine the effect of Rashba spin-orbit coupling and in-plane magnetic field on the superconductivity induced by placing superconducting contacts on the sample when there is a finite density of carriers in the bulk.

1.2 Organization of the dissertation

The thesis is divided into four chapters. In the remainder of this first chapter, background information for the rest of the work is presented.

In chapter 2, we discuss charge sensing in the $\nu = 5/2$ fractional quantum Hall state. In such a system, the quasiparticles carry a charge of $e/4$, and the degeneracy of the topological state contributes a non-zero entropy to the system. We demonstrate that a charging diagram of the system as a function of chemical potential and temperature contains evidence of this entropy, and furthermore, that when two quasiparticles are trapped near each other by disorder, they can split the degeneracy. This splitting of the degeneracy is visible in the charging diagrams we consider. We also present a new contribution to the splitting of the degeneracy of the topological ground state, due to the orbit of confined quasiparticles in a circular potential well.

Chapter 3 presents a detailed analysis of changes in electron number parity for semiconducting one-dimensional wires, with strong spin-orbit coupling, and with proximity-induced superconductivity. We show how the locations of parity flips in the chemical potential - magnetic field plane depend on the system parameters. The Majorana state carries no charge when the ends are infinitely separated, but carries

a finite charge when the wavefunctions, which are concentrated at the ends, begin to overlap. We demonstrate that although the Majorana wavefunctions are peaked at the ends, the associated charge is uniformly distributed along the wire. Furthermore, we address the magnitude of the change in total charge associated with the flip in parity in both the topological and non-topological cases. We also consider the effects of electron-electron interactions, and make predictions and recommendations for future experiments.

In chapter 4, we examine the dependence of induced superconductivity in 2D systems on in-plane magnetic fields and Rashba spin-orbit coupling, motivated by recent experiments on HgTe. In particular, we show how superconductivity induced from superconducting contacts depends on the separation between the contacts, the strength and direction of the applied external magnetic fields, and spin-orbit coupling.

1.3 Topological Physics

In the words of Leon Balents, "topology, the mathematical description of the robustness of form, appears throughout physics, and provides strong constraints on many physical systems" [1]. This robustness can be described elegantly through constructions such as the Chern number. However, we will do without such definitions for the presentation here. For the topics covered in this thesis, the movements of quasiparticles around each other, and in particular, the topology of such motion is robust. In other words, we are not concerned with the exact path one particle takes around another, but with the number of times encircling occurs and the order in which these take place. We begin with a review of non-Abelian anyon braiding statistics, and

continue with a brief discussion of topological quantum computers before discussing the specific systems addressed in the remainder of the thesis.

1.4 Anyons

Classically, when two identical particles interchange positions, the system does not change. Quantum mechanically, we know that the wave function of two particles obtains a phase when the particle positions are switched. Note that performing the swap twice is equivalent to taking one particle around the other. Since, in three spatial dimensions, this circular path can be deformed to a point, the system must return to its initial state after the double interchange. Therefore, the effect of one interchange must square to one, and the phase is either zero or π. We call the zero case Bosons, and the π case Fermions, and this distinction in how the particles behave under interchange is the foundation for many of the fascinating results of quantum mechanics, starting with the Pauli exclusion principle.

If we now imagine a system confined to only two spatial dimensions and perform the same double interchange as above, we note that the loop one particle makes around the other is confined to the plane. We therefore cannot contract it to a single point without passing through the other particle, and the system, therefore, does not necessarily return to its initial state. Without a constraint on the phase, we see that particles in two dimensions can, in principle, have *any* phase under interchange, and we call such particles that are neither Bosons nor Fermions *anyons*. In particular, these particles are anyons with statistics θ, where $e^{i\theta}$ is the extra phase the wavefunction picks up when we interchange two particles in a clockwise manner.

This was first discussed in [2, 3].

Although predicted to exist in two-dimensional systems, can anyons actually exist in a physical system constructed out of the standard Bosons and Fermions of our three-dimensional world (e.g. electrons, protons, neutrons)? Shockingly, the answer is yes, and fractional statistics were first observed for the elementary quasiparticles in fractional quantum Hall states [4]. We discuss how systems can be built in the lab that are *effectively* low dimensional in section 1.10.

1.5 Non-Abelian Anyons

More recently, it was discovered that quasiparticles in certain quantum Hall states can exhibit even more amazing behaviour under interchange than the Abelian anyon phases discussed above. These are non-Abelian anyons, and we present details in this section.

1.5.1 The Braid Group

In order to understand non-Abelian statistics, we first define the braid group, $\mathbb{B}_N$, which acts on our Hilbert space. Consider N particles, initially at positions $\{x_i\}_{i=1..N}$ in a plane. To pictorially understand the braid group, consider a plane with time as the third axis, as in figure 1.1. As time progresses, the particles (may) move around each other, and their world lines twist and braid.

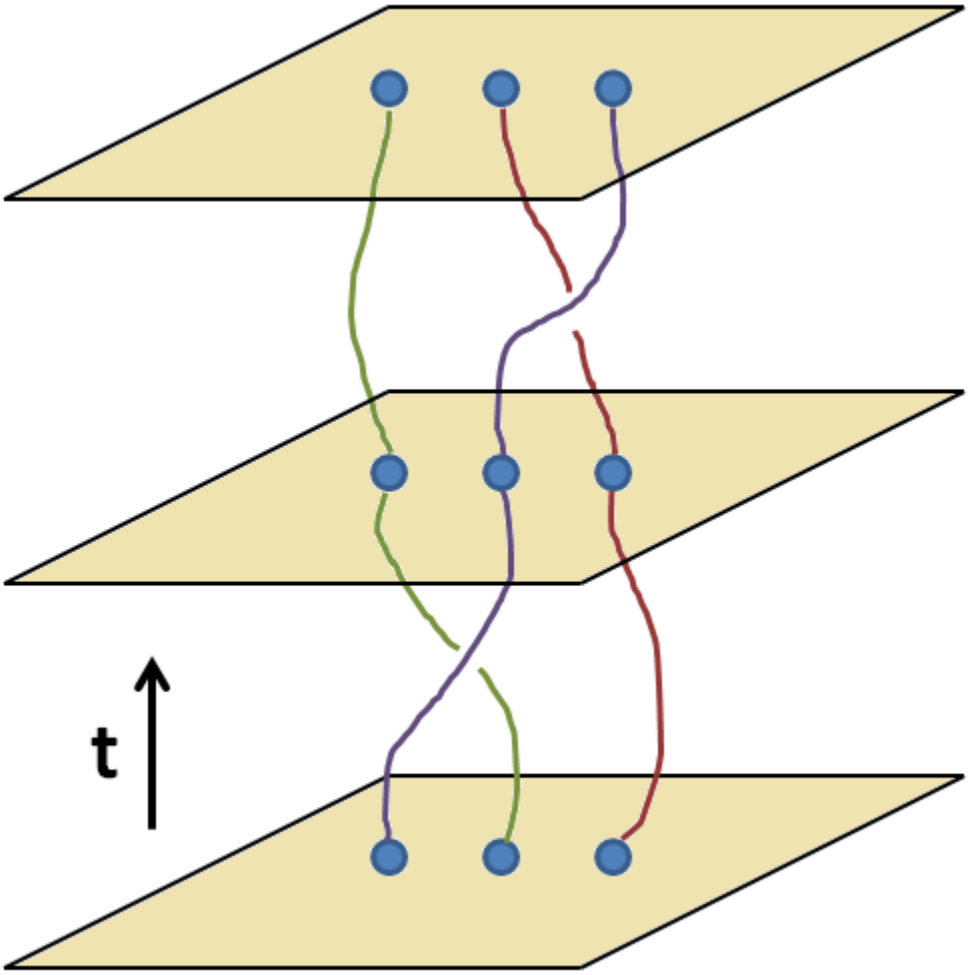

Figure 1.1: World Lines. The positions of three quasiparticles in a plane are shown as a function of time. The world lines of the quasiparticles can braid, and in two dimensions the braids cannot be continuously deformed into non-braiding lines.

1.5.2 Non-Abelian Braiding Statistics

For a system of quasiparticles at a given set of positions, there exists a degenerate set of ground states of degeneracy g. Braiding the particles can interchange these ground states, and corresponds to unitary transformations on the degenerate set of states. The effects of the interchange on the ground state are determined by the topology of the braid group, and this forms a representation of the braid group. If any pair of these g-dimensional matrices do not commute, then the representation is non-Abelian, and the particles in the ground state obey non-Abelian statistics. It is known that within this set of states, no local perturbation can have finite matrix elements, at least at low energies [5].

1.5.3 Fusion

In chapter 2, we will be interested in the case where two particles are close together, which brings us to the topic of fusion. We note that a system that contains anyons can, in general, support different types of anyons, i.e. anyons of different phases. Furthermore, if two anyons are brought close together, they could form a bound state with different statistics. Fusion describes the rules for what new anyon is created when two anyons are brought together.

For non-Abelian anyons, each fusion process can have multiple end states, and we call these the fusion channels. The different fusion channels can be used to account for the degenerate ground state of a system of non-Abelian anyons, and we will use this approach below in our discussion of quasiparticles in the $\nu = 5/2$ fractional quantum Hall state.

For the case of $\nu = 5/2$ that we will be interested in below, the system supports three types of anyons, which we label $\mathbf{1}$, σ, and ψ. The fusion rules for these anyons are

$$\sigma \times \sigma = \mathbf{1} + \psi, \qquad \sigma \times \psi = \sigma, \qquad \psi \times \psi = \mathbf{1},$$
$$\mathbf{1} \times \sigma = \sigma, \qquad \mathbf{1} \times \psi = \psi, \qquad \mathbf{1} \times \mathbf{1} = \mathbf{1}. \tag{1.1}$$

The most important rule is the first, which shows that two σ's can fuse into two distinct fusion channels. If we create four σ's from one electron (reasons for this will become clear below), we must have a net state of $\mathbf{1}$, since the electron initially has no topological charge. We see that there are two ways for this to happen, namely that each pair of σ's fuse to ψ, or each pair fuses to $\mathbf{1}$. For four σ's, we thus have a degeneracy of two in the ground state. More generally, for N σ's, we have a degeneracy of $g = 2^{N/2-1}$. This will be essential for the discussion in chapter 2.

Another relevant fact about these anyons, necessary to understand the results in chapter 2 is that braiding two fused-particles around each other does not change their fusion channel. This must be true, since the net topological charge can be measured on any loop that encircles the two particles [5]. Braiding two anyons that have fused to one fusion channel is thus equivalent to braiding two Abelian anyons, and the result is an additional phase. If there are additional particles involved in the braiding, then the fusion channel can be changed. In particular, as shown in figure 1.2, if quasiparticles A and B are fused, then taking quasiparticle D along path number one will change the fusion channel of A and B, whereas taking D on path two will not change the fusion channel of A and B. Note that when the fusion channel of A and B changes, so does the fusion channel of C and D.

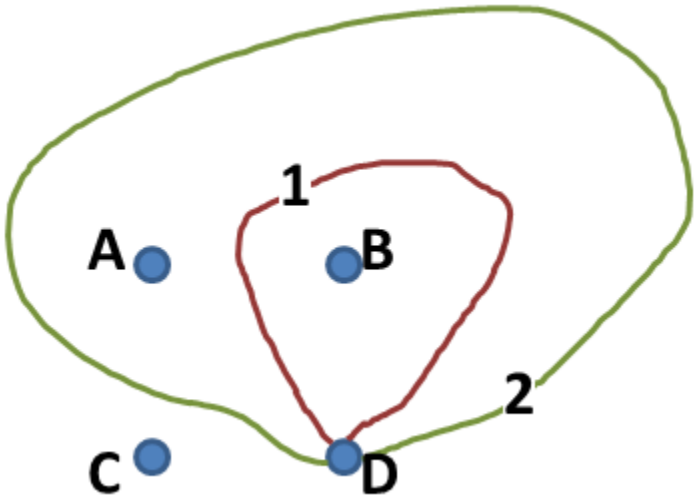

Figure 1.2: Braiding of fused particles. Assume A and B are fused, and C and D as well. Bringing D around loop 1 changes the fusion channel, whereas loop 2 does not.

Furthermore, bringing two anyons close to each other splits the degeneracy between the available fusion channels, and leaves one energetically favourable. As we discuss in chapter 2, if two quasiparticles are trapped in a single well under conditions where the quantum mechanical zero-point motion causes the quasiparticles to move around each other, this can give rise to an additional splitting of the energy between the fusion channels. This contribution to the splitting is above and beyond the splitting due to proximity of individually localised quasiparticles.

1.6 Topological Quantum Computers

Although this thesis is not about quantum computing, the construction of a topological quantum computer is an important source of inspiration and motivation for research on topological systems. We therefore provide a (very brief) description

of how a topological quantum computer might work.

For a topological quantum computer, the qubits correspond to the choice of fusion channels for two particles. Since these particles are by definition well separated – otherwise the choice of fusion channel would be unique – the qubit is *non-local*. Information can be encoded by braiding several quasiparticles, and measurements occur when two quasiparticles are brought close together. Since the qubit is non-local, it is resistant to errors due to local perturbations. Errors can occur, however, if additional quasiparticles appear in and move through the system. Possible sources for additional particles are thermal activation, and local potential traps. However, by creating a system with a large gap and minimal disorder, such errors can be avoided, and the non-local qubits leave us with a fault-tolerant computer. It is this tolerance of errors that make topological systems such an exciting route in the search for quantum computers [5].

1.7 $\nu = 5/2$ FQHE

The quantum Hall effect is fascinating, in both its integer and fractional forms. Here we present a quick summary of important ingredients, and information relevant to the work in this thesis. Although there are many books and review papers on the subject, the three sources that proved most useful in the preparation of the research and this discussion are [5–7].

1.7.1 Electrons in 2D & Magnetic Fields

When non-interacting electrons are confined to two spatial dimensions and an external magnetic field is applied, the Hamiltonian of the system is

$$H_0 = \frac{1}{2m_e}\left(\vec{p}_i - \frac{e}{c}\vec{A}(\vec{x}_i)\right)^2. \tag{1.2}$$

where $\vec{p}$ is the momentum, e the electron charge, m_e the electron mass, c the speed of light, and $\vec{A}$ the vector potential which is a function of position. The eigenstates of this Hamiltonian are split into Landau levels, each containing many degenerate states. The Landau levels are all equally spaced in energy. The splitting between these levels is $\hbar\omega_c = \hbar eB/m_e c$, where $\hbar$ is the reduced Plank's constant, and B the applied magnetic field.

If we choose the symmetric gauge, with $\vec{A} = \frac{B}{2}(-y, x, 0)$ for an applied field in the z-direction perpendicular to the plane, then we can make the substitution $z = x - iy$, and find a basis for the states in the lowest Landau level:

$$\psi_m = (2\pi 2^m m!)^{-1/2} z^m e^{-z\bar{z}/4\ell_B}. \tag{1.3}$$

Ignoring the Gaussian factor, the eigenstates are analytic polynomials in z. The denominator in the exponent includes the magnetic length, $\ell_B = \sqrt{\hbar c/eB}$, which corresponds roughly to the radius of a circle occupied by one electron. The basis, and in particular the magnetic length, will be important in our later analysis of trapped quasiparticles in chapter 2.

Still in the symmetric gauge, we can find the degeneracy as follows. Consider a disk or radius R. From the wavefunctions, we find (by taking a derivative with respect to z) that the maximum occurs along a circle of radius $r = \sqrt{2m}\ell_B$. We

can thus fit all eigenstates with $m \leq R^2/(2\ell_B^2)$ into this disk, which is the number of states. The degeneracy is then the number of states divided by the area, which gives $g = 1/(2\pi\ell_B^2) = eB/hc = B/\phi_0$, with $\phi_0 = hc/e$ the magnetic flux quantum. We then define the filling factor as the ratio of the density to the degeneracy:

$$\nu = \frac{\rho}{g} = 2\pi\ell_B^2\rho = \frac{\rho\phi_0}{B}. \tag{1.4}$$

When the chemical potential sits between Landau levels, the longitudinal resistivity vanishes, and the Hall resistivity is

$$\rho_{xy} = \frac{h}{\nu e^2}, \tag{1.5}$$

where ν is quantised (integer or fraction). ν corresponds to the filling factor of the Landau levels, which, when the chemical potential is between levels, is an integer.

This non-interacting picture can be used to understand the integer quantum Hall effect. We next look at the phenomena associated with the inclusion of Coulomb interactions.

1.7.2 Interactions and Fractions - 5/2

In the previous section, we ignored Coulomb interactions. This is a reasonable assumption when Landau levels are filled, and the spacing to the next Landau level, $\hbar\omega_c$ is much larger than the scale of the Coulomb energy, e^2/ℓ_B. However, when a Landau level is only partially filled and the chemical potential is inside the Landau level, electron-electron interactions need to be included.

Various works [8–10] describe series of fractionally filled states expected to exhibit quantum Hall plateaus with fractional values of ν. Approximate wavefunctions

have been written down for these states, and their accuracy has been checked through numerical calculations. One reason why these are not exact wavefunctions is that they neglect the small but non-zero size of real systems in the direction perpendicular to the plane. Most of the expected, and observed, fractional quantum Hall states have odd denominators. One outsider to this group, first observed in 1987 [11], is the $\nu = 5/2$ state

Several wavefunctions have been written down for this unexpected even-denominator state. A trial wavefunction of particular interest, which we assume to be a valid description of the state in the work presented in chapter 2, is the Moore-Read (MR) Pfaffian [12]:

$$\Psi_{\rm Pf} = {\rm Pf}\left(\frac{1}{z_i - z_j}\right)\prod_{i<j}(z_i - z_j)^m \exp\left(-\sum_i |z_i|^2/4\ell_B^2\right). \tag{1.6}$$

The first term, the "Pfaffian", is the square root of the determinant, defined for an anti-symmetric matrix. When m is even, this describes an even-denominator state in the lowest Landau level. Although the MR state is only an approximate ground state for Coulomb interactions, it is interesting to note that it is an exact ground state of a three-body repulsive interaction. Since topological properties cannot change when we perturb the wavefucntion unless the gap closes, and since small perturbations will not close the gap, the MR state can be used to describe the topological features of the system. It has been shown [12] that the quasiparticles in a MR state should have non-Abelian statistics. The fusion rules are as described in section 1.5.3, and for N quasiparticles, the degeneracy of the ground state is $2^{N/2-1}$. The anyonic quasiparticles fall into the class of Ising$\times\mathbb{Z}_8^{(1/2)}$, as described in [13].

An alternate wavefunction is the anti-Pfaffian, which is the particle-hole conju-

gate of the MR state [14,15]. Both the MR and the anti-Pfaffian have the same energy in a lowest Landau level calculation, and it is therefore difficult to determine which is the better approximation for the true 5/2 state. However, quasiparticles in both states have the same interesting properties we assume for the rest of our discussion (e.g. non-Abelian statistics, fractional charge), and so we do not need to distinguish between the two states.

In 2000, Read and Green [16] showed that the MR state is the quantum Hall analog of a spin polarised $p_x + ip_y$-wave superconductor. In the $p_x + ip_y$ superconductor, the vortices have Majorana modes attached to them, and the vortices play a role similar to the quasiparticles in the $\nu = 5/2$ state. This analogy can be useful in picturing the topological charge as an exponentially decaying wavefucntion centred on the quasiparticles, and the splitting between fusion channels as a result of overlap of the wavefunctions.

Other proposed states include the Halperin (3,3,1) state [17]. Although alternative wavefunctions remain possible explanations for states at half-filled Landau levels, numerical calculations [18, 19] suggest that these other states are not favoured at $\nu = 5/2$. We note, however, that these numerical calculations are performed for small numbers of electrons ($N \leq 18$), on a sphere or a torus, and therefore further experimental evidence is required.

1.7.3 Fractional Charge and SETs

One of the predictions of Moore and Read [12] is that the quasiparticles in the $\nu = 5/2$ state carry a charge of one quarter the electron charge. Fractional charge

had already been predicted and measured in other fractional quantum Hall states [8, 20–22]. In fact, recent experiments seem to show that the quasiparticles really do have charge $e/4$ [23–25]. Here, we briefly focus on the work by Venkatachalam *et. al.* [23], which is the inspiration for our investigations on the subject. The experiment in [23] uses a Single Electron Transistor (SET) to measure the charge of the 5/2 quasiparticles. A SET is a quantum dot formed between two metallic leads, and capacitively coupled to the system under study. The appearance of additional charges in the area under the SET changes the electric potential in the dot, and consequently the current through the dot. By continuously varying the chemical potential (μ) in the sample, say by a global back-gate, and measuring the change in density (n) with the SET, the compressibility, $\partial n/\partial \mu$ can be obtained. Further details on SETs are presented clearly in [26].

1.8 1D wires

Another system predicted to host Majorana modes that has gained much attention, including our own, is the quasi-one-dimensional semi-conducting wire with spin-orbit interactions coupled to a superconductor. Preceded by the idea of a two-dimensional semi-conductor sandwiched between a s-wave superconductor and a magnetic insulator [27], the one dimensional system was proposed in 2010 [28, 29]. The 1D version is simpler than the 2D version because it replaces the magnetic insulator with an applied magnetic field, and removes the need for vortices, which could cause decoherence [28].

These wire systems have been created and measured by several experimental

groups [30–36], who have tried various combinations of materials for the semiconductor and superconductor. The Majorana states are confined to the ends of the wire, and in a purely one dimensional system cannot be braided around each other. A solution to this problem was provided in [37, 38], where the authors suggested a network of wires, in which the "end" of the wire is moved using external gates, so that the Majorana states can be braided.

1.8.1 Bogoliubov de Gennes

In chapters 3 and 4, we use the Bogoliubov de Gennes (BdG) formalism. We therefore provide a quick description here. To understand the BdG Hamiltonian, we begin with non-interacting electrons with a spin degeneracy, described by:

$$H_0 = \left(\frac{(-i\nabla)^2}{2m} - \mu(x) \right) \sigma_0, \tag{1.7}$$

where m the mass, and σ_0 is the identity matrix in spin-space. Here $\mu(x)$ is the local chemical potential, which may depend on position in the presence of a spatially varying external potential. Later, we will generalise the Hamiltonian to include magnetic fields and spin-orbit interactions.

We can write this Hamiltonian in second quantised notation for many particles as:

$$H_0 = \sum_\sigma \int d\vec{x} c_\sigma^\dagger(\vec{x}) \left(\frac{(-i\nabla)^2}{2m} - \mu \right) c_\sigma(\vec{x}), \tag{1.8}$$

where $c_\sigma^\dagger(\vec{x})$ is the creation operator for an electron with spin σ and position $\vec{x}$. We can (for reasons that become clear in a moment) write this as

$$H_0 = \frac{1}{2} \sum_\sigma \int d\vec{x} \left[c_\sigma^\dagger(\vec{x}) \left(\frac{(-i\nabla)^2}{2m} - \mu \right) c_\sigma(\vec{x}) - c_\sigma(\vec{x}) \left(\frac{(-i\nabla)^2}{2m} - \mu \right) c_\sigma^\dagger(\vec{x}) \right], \tag{1.9}$$

where we used the Fermion anti-commutation relation and discarded a constant term. Next, we introduce a spinor $\psi(\vec{x}) = \left(c_\uparrow(\vec{x}), c_\downarrow(\vec{x}), c_\uparrow^\dagger(\vec{x}), c_\downarrow^\dagger(\vec{x})\right)^T$, and we can write the Hamiltonian as $H_0 = \int d\vec{x}\psi^\dagger(\vec{x})H_{BdG}\psi(\vec{x})$, where

$$H_{BdG} = \frac{1}{2}\begin{pmatrix} \zeta & 0 & 0 & 0 \\ 0 & \zeta & 0 & 0 \\ 0 & 0 & -\zeta & 0 \\ 0 & 0 & 0 & -\zeta \end{pmatrix} \tag{1.10}$$

and we used $\zeta = \frac{(-i\nabla)^2}{2m} - \mu(x)$. Note that we have, until now, simply added redundancy and doubled our spectrum. The added advantage comes when we add a pairing term to the Hamiltonian, which in this formalism simply couples the top and bottom blocks of the Hamiltonian. In particular, if we consider a conventional s-wave singlet pair potential, $H_\Delta = \int d\vec{x}\left[\Delta(\vec{x})c_\uparrow^\dagger(\vec{x})c_\downarrow^\dagger(\vec{x}) + \Delta^*(\vec{x})c_\downarrow(\vec{x})c_\uparrow(\vec{x})\right]$, then our Hamiltonian is $H = H_0 + H_\Delta$, and we can write the BdG Hamiltonian as

$$H_{BdG} = \frac{1}{2}\begin{pmatrix} \zeta & 0 & 0 & \Delta(\vec{x}) \\ 0 & \zeta & -\Delta(\vec{x}) & 0 \\ 0 & -\Delta^*(\vec{x}) & -\zeta & 0 \\ \Delta^*(\vec{x}) & 0 & 0 & -\zeta \end{pmatrix}. \tag{1.11}$$

We can write the Schrödinger equation for this Hamiltonian, which we call the BdG equation:

$$H_{BdG}\vec{\Phi} = E\vec{\Phi}, \tag{1.12}$$

with eigentstates $\vec{\Phi} = (u_\uparrow(\vec{x}), u_\downarrow(\vec{x}), v_\uparrow(\vec{x}), v_\downarrow(\vec{x}))^T$

After performing a unitary transformation, we may define operators

$$\gamma_\uparrow(\vec{x}) = u_\uparrow(\vec{x})c_\uparrow(\vec{x}) + v_\downarrow^*(\vec{x})c_\downarrow^\dagger(\vec{x}) \tag{1.13}$$

$$\gamma_\downarrow(\vec{x}) = u_\uparrow(\vec{x})c_\uparrow(\vec{x}) - v_\downarrow^*(\vec{x})c_\downarrow^\dagger(\vec{x}). \tag{1.14}$$

The corresponding operators satisfy $[\gamma_\sigma(\vec{x}), H_0] = E\gamma_\sigma(\vec{x})$. When the system is translationally invariant, i.e. $\mu(x) = \mu$ and $\Delta(x) = \Delta$, we can impose periodic boundary conditions and assume plane wave solutions. After Fourier transforming, the spectrum has two pairs of degenerate solutions,

$$E_\pm = \pm\sqrt{\zeta_k^2 + |\Delta|^2}, \tag{1.15}$$

and the system is gapped whenever $|\Delta| \neq 0$.

In general, the eigenstates of H_{BdG} will be mixtures of electron and hole states. The ground state of H_{BdG} is a filled Fermi sea, with all negative energy states filled, and all positive energy states empty. Excitations are then described by mixtures of creation and annihilation operators, or electrons and holes, with the weighting between the two more equal at lower energies. We can calculate matrix elements with these excited mixed states, and one finds that terms of the form $\langle c_\uparrow c_\downarrow \rangle$ can have non-zero expectation values, even in the ground state.

1.9 HgTe

1.9.1 Topological Insulators

We are interested in HgTe, an example of the recently discovered class of materials known as two-dimensional topological insulators [39–46]. These states are some-

times referred to as quantum spin Hall conductors, although they only have finite spin Hall conductance when the z-component of the spin is preserved. When system parameters are tuned properly, these materials have no excitations in the bulk, and modes of opposite spins moving in opposite directions along the edges. These edge modes are gapless in the absence of a coupling that breaks time-reversal symmetry. When the edges are coupled to a superconductor, Majorana modes are predicted to be present on the edge. In this thesis, we do not address the presence of Majorana modes – we seek to understand whether or not superconductivity can be induced throughout a sample coupled to a superconductor on its edge.

1.9.2 Induced Superconductivity

Recent experiments have shown that it is indeed possible to proximity-induce superconductivity in HgTe quantum wells [47]. Superconducting titanium/aluminium contacts are placed on the sample, and a supercurrent is observed. When the system is in the topological regime, the current flows in edge states. In order to form localised Majorana Fermions, an in-plane field must be applied, and we will examine how this field changes the induced superconductivity in the HgTe.

1.10 Real Systems

The systems discussed in this thesis are one- or two-dimensional, but our world has three spatial dimensions. How do experimentalists create effectively low-dimensional systems? For the cases we study, they grow semiconducting heterostructures and nanowires. A heterostructure is a layered combination of several semiconducting ma-

terials. The most common example for quantum Hall experiments is a mix of GaAs and $Al_xGa_{1-x}As$, where the GaAs is sandwiched between two much thicker layers of AlGaAs. Typical thicknesses for the thin layer are on the order of 10nm. Since GaAs has a smaller bandgap than AlGaAs, electrons in the filling of the sandwich are trapped. For this particular choice of materials, holes are also trapped since both the valence and conduction bands are shifted toward a smaller bandgap in GaAs. By keeping the GaAs layer extremely thin, motion in the perpendicular direction becomes quantised. If only the lowest level in this direction is occupied, the system is effectively two-dimensional.

Various techniques exist for growing such materials, as well as for gating and contacting them. Details are available in [48]. In some cases, dopants are placed within the AlGaAs, to increase the density of the two-dimensional gas. As discussed in chapter 2, these ionised dopants can also cause disorder. A sketch of these systems is shown in figure 1.3

Although wires can be created by growing a two-dimensional system and then confining it to one dimension with metallic gates, the wires used in experiments we discuss in chapter 3 were grown as wires. Long pillars of InAs or InSb are grown in the lab, and then the best ones are knocked over onto a substrate and placed over the necessary gates. Recently developed techniques allow for superconducting shells to be grown directly on these pillars [49].

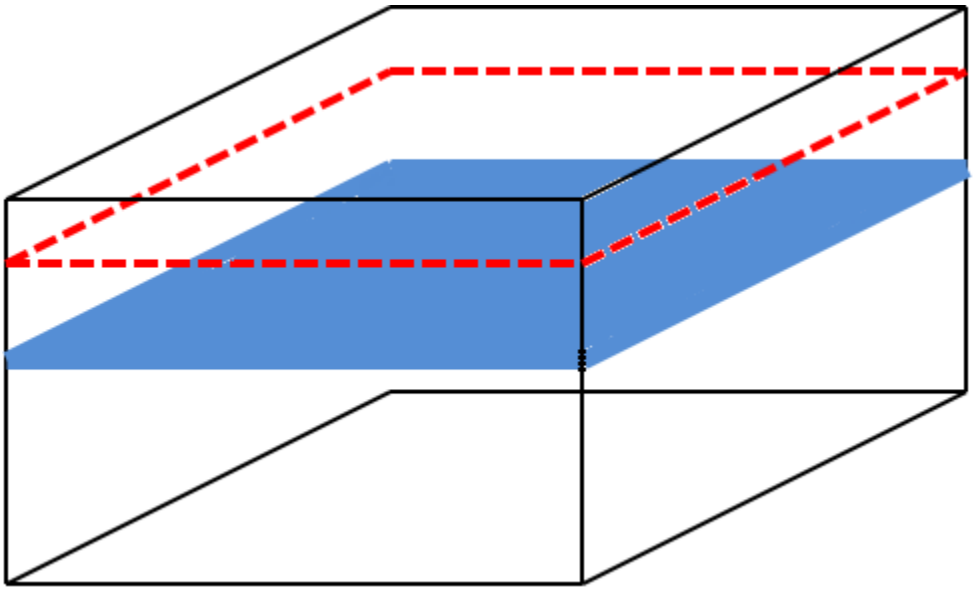

Figure 1.3: A sketch of a AlGaAs/GaAs heterostrcutre. The blue plane represents the thin layer of GaAs in the large block of AlGaAs. The red dashed lines mark the plane in which dopants are often placed.

Chapter 2

Detecting Non-Abelian Anyons by Charging Spectroscopy

2.1 Overview

Observation of non-Abelian statistics for the $e/4$ quasiparticles in the $\nu = \frac{5}{2}$ fractional quantum Hall state remains an outstanding experimental problem. The non-Abelian statistics are linked to the presence of additional low energy states in a system with localised quasiparticles, and hence an additional low-temperature entropy. Recent experiments, which detect changes in the number of quasiparticles trapped in a local potential well as a function of an applied gate voltage, V_G, provide a possibility for measuring this entropy, if carried out over a suitable range of temperatures, T. We present a microscopic model for quasiparticles in a potential well and study the effects of non-Abelian statistics on the charge stability diagram in the $V_G - T$ plane, including broadening at finite temperature. We predict a measurable slope for the

first quasiparticle charging line, and an *even-odd* effect in the diagram, which is a signature of non-Abelian statistics.

2.2 Introduction

The unambiguous observation of particles obeying non-Abelian statistics remains an outstanding experimental challenge in condensed matter physics. The Moore-Read (MR) fractional quantum Hall state (FQH) [12], believed to be realised at filling fraction $\nu = 5/2$, is one of the most promising candidate phases to exhibit such quasiparticles (QPs) [5]. The MR state is predicted to support QPs of charge $\pm e/4$; for N such QPs, localised and well separated from each other, there should be a nearly degenerate set of ground states, with multiplicity $2^{N/2-1}$. For temperature T larger than the splitting of these ground states, but smaller than the gap to higher excited states, this degeneracy contributes an effective entropy to the system, the *non-Abelian entropy*.

Non-Abelian statistics predicts that pairs of QPs can interact to form two distinct states, or *fusion channels*, f, commonly denoted as $f = 1,\ \psi$. In a finite system, the two states have different energies, and the ground state is unique; for T below the splitting between the two, the non-Abelian entropy is lost.

There are several recent theoretical proposals for techniques to observe this entropy through bulk measurement of thermodynamic and transport properties [50–53]. Recent measurements in this direction of thermoelectric response at $\nu = 5/2$ are encouraging [54]. These theoretical proposals assume that all QPs are well separated, such that degeneracy-lifting interactions are weak or non-existent. However,

recent local electronic charge-sensing measurements, using a single-electron transistor (SET) [23], suggest that QPs tend to trap in local potential wells due to electrostatic disorder, which may be tightly confining and contain more than one QP. In this experiment, by comparing the spacing between charging events at $\nu = 5/2$ with those at 7/3, the QP charge was verified to be $e/4$ as predicted. Confined QPs split their degeneracy through two means: Majorana exchange [55, 56], present even for stationary QPs, and as we show here, an orbital splitting from interchange of the charged QPs, which can dominate in special cases.

In this chapter, we study the charging spectra of local quasiparticle traps. Such traps may be induced by disorder or defined by gates. Their spectra reflect the QP statistics, just as electronic dot spectra reflect the spin and Fermionic statistics of electrons. We show that low-frequency SET charge-sensing measurements, which provide only thermally-averaged information regarding the dot spectra, are sufficient for extracting non-Abelian signatures. At low but experimentally accessible T, we predict a robust temperature evolution of the $N = 0 - 1$ transition, and an even-odd effect in the evolution of the charging spectrum for several non-Abelian anyons. This effect should be visible for T below the relevant gaps to excited states for N particles, which we calculate for $N = 1, 2$.

The experiments of [23] measure the change in potential at the SET induced by a change δV_G in the potential applied to a backgate on the sample. If there is a single disorder-induced well close to the SET, the measured signal is inversely proportional to the compressibility of the well, $\kappa = \frac{\partial \langle N \rangle}{\partial \mu}$, where μ is the QP chemical potential in the vicinity of the well. For an isolated well, the relation between δV_G and the change

in μ should be linear, but the constant of proportionality is geometry-dependent, as screening depends on the local environment as well as the distance to the gate. If there are several wells nearby, their signals are weighted according to the strength of their coupling to the SET; in this case, Coulomb interactions between wells need also be taken into account.

At $T = 0$, the compressibility has a δ-function peak at a crossing of energy levels between N and $N + 1$ QPs in a well. At finite T, the peak broadens and may shift as a function of μ due to entropy effects. The simplest case to consider is an isolated well at the transition from $N = 0$ to $N = 1$, or slightly more involved, from one to two. At higher occupation numbers, we give qualitative arguments for the stability diagram. We examine both circular and elliptical traps, and account for temperature effects including broadening and excited states. In our model, $e/4$ QPs are represented as interacting charged particles in a magnetic field, confined to the lowest Landau level (LLL), with non-Abelian statistics. The interaction is Coulomb, supplemented by an interaction $V_X(r)$ due to the exchange of Majorana Fermions.

2.3 Qualitative Picture

We begin with the charging diagram for Abelian particles in a well, to contrast it with the non-Abelian case. For simplicity of presentation, we consider varying only the QP chemical potential, although as discussed below, local gating will be required to access the full charging spectrum. The well sits in a larger quantum Hall state containing other distant wells, which provide a reservoir for QPs. At $T = 0$, as a function of chemical potential, a series of peaks in the compressibility appear,

corresponding to individual charging events in the well. The spacing of these peaks defines the charging energy, $U(N)$. As T increases, the peak centres evolve vertically in the charging diagram (red dashed lines in Fig 2.1), until T reaches the minimum excitation energy, Δ_N, set by the excited states within the well. Above this energy,

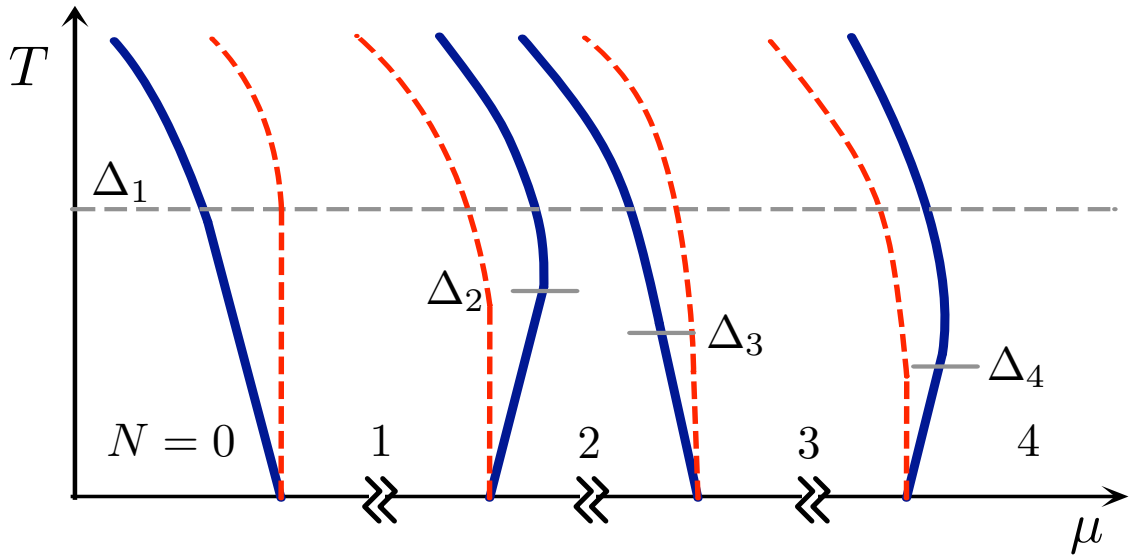

Figure 2.1: Cartoon charge stability diagram, showing only peak centres (no broadening). Vertical axis is temperature T; horizontal axis μ is the chemical potential for charged QPs, controlled in experiment by a gate potential. Red dashed lines are for Abelian particles. Blue solid lines correspond to non-Abelian QPs in a tightly confining well. Δ_N is the gap to excited states for N particles, and sets scale for other entropic effects. Notice even-odd effect for non-Abelian anyons.

the curve deviates from a straight line due to entropic effects. The peaks broaden linearly with T for both Abelian and non-Abelian QPs.

When several non-Abelian QPs occupy a tightly confining well, they uniquely fuse at low energies. This produces a distinct experimental signature - the *even-odd* effect. As highlighted in [51], the density dependence of the zero-temperature entropy produces a distinct signature in the inverse compressibility of bulk samples at low T.

In local traps with discrete QP number, the difference in zero-temperature entropy ΔS between adjacent number states produces a related low-T signature in the charge stability diagram: the slope of the charge transition line in the $\mu - T$ plane is $-1/\Delta S$. The first QP placed in the well contributes $S_{NA} = \ln 2/2$ to the non-Abelian entropy ($k_B = 1$), or equivalently adds a $\sqrt{2}$ degeneracy; thus, the $N = 0 - 1$ transition line has slope $-2/\ln 2$ in the $\mu - T$ plane as $T \to 0$. A second QP fuses uniquely with the first QP into the 1 or ψ channel and the non-Abelian entropy is extinguished, $\Delta S = -\ln 2/2$. Thus, as T increases from zero, the $N = 1$ state becomes entropically more favourable than the $N = 2$ state, and the transition line has slope $+2/\ln 2$ (blue solid lines in Fig 2.1). This even-odd effect persists as the well charges: odd numbers of particles fuse into the non-Abelian σ-channel, while even numbers uniquely fuse into either the Abelian 1 or ψ channels, as long as T remains below the splitting between these two channels. If the splitting between channels is smaller than Δ_N, there exists an intermediate regime, in which the degeneracy is preserved and the non-Abelian entropy increases by $\ln 2/2$ with every additional particle, and all lines have parallel negative slopes. A similar effect for electrons due to spin degeneracy was predicted and seen in quantum dots at $B = 0$ [57, 58]. For a quantised Hall state in a strong magnetic field, however, if QPs have more than one spin state, we expect their energies to split, due to the Zeeman and/or Coulomb exchange fields, by an amount large compared to the temperatures of interest. Moreover, if spin-degeneracy were present, the charging lines would have a different slope than for fusion channel degeneracy, because of the factor of two difference in entropy per QP.

For wells far apart compared to the magnetic length, the rate, $\delta_{\text{well}}/\hbar$ of Majo-

rana exchange between them falls off exponentially in their separation. We therefore consider charging lines for temperatures $T \gg \delta_{\text{well}}$, assumed zero for an isolated well. In this limit there is no fusion-channel splitting between wells, and each independently exhibits the even-odd effect. However, the charging spectra are not completely independent due to capacitive coupling. In an experiment sensitive to multiple disorder-induced wells, the charging spectra of the wells appear overlaid with unknown offsets making the even-odd effect more difficult to observe, without first associating the various peaks to their respective wells. Experiments [23,59,60] suggest that determining such associations is possible.

2.4 Equilibration

Although QPs are locally trapped, the equilibrium model we present requires that the system explores the degenerate ground state manifold faster than the measurement time t_{exp} of the charge-sensing experiments. This time is determined by the rate of change of the gate voltage, typically $t_{\text{exp}} \sim 0.1\text{s}$. We estimate the equilibration time due to thermal excitations as $t_{\text{T}} \sim 10^{-4}\text{s} \ll t_{\text{exp}}$, meeting the requirement. To obtain this estimate, we take $t_T = \hbar/E_{\text{T}}$, where $E_{\text{T}} \sim \Delta_{5/2} \exp\left(-\Delta_{5/2}/k_B T\right)$ is an Arrhenius estimate of thermally-induced inter-well hopping. Taking an activation gap of $\approx 0.25\text{K}$ and a temperature of 20mK, we obtain $t_T \sim 10^{-4}\text{s}$. t_{exp} is an experimental parameter, typically of order 10 Hz in existing measurements [23]. Moreover, the observed changes in the charge state of the studied well during experiments [23] imply that QPs hop freely between wells on the time scale t_{exp}. Assuming the hopping processes have a stochastic component, they will naturally lead to braiding of QPs

from different wells.

2.5 Quantitative Picture

Returning to a single well in a large bath, we present a model for calculating the charging diagram. The partition function is

$$Z = \sum_N g(N) e^{-\beta(F(N,T)-\mu N)}, \tag{2.1}$$

where $\beta = 1/T$, the internal free energy of N-particle states in the well is $F(N,T)$, and

$$g(N) = \begin{cases} \sqrt{2} & N \text{ odd} \\ 1 & N \text{ even} \end{cases} \tag{2.2}$$

captures the non-Abelian degeneracy associated with net fusion within the well. In a well where QPs are close, such that all other fusion-degeneracies are split by energies larger than T, we take $F(N,T) \approx F(N,0)$ for $T \ll \Delta_N$, the gap to excitations. In principle, however, for a wide well where electron-electron interactions localise the QPs further apart, an intermediate regime can exist in which the topological degeneracies are not significantly split and $F(N,T) \approx F(N,0) - T\lfloor \frac{N}{2} \rfloor \ln 2$, where $\lfloor \cdot \rfloor$ denotes the integer part, for temperatures up to the gap Δ_N.

The compressibility follows from the partition function. To leading order near the $N-1$ to N charge transition at the critical chemical potential, $\mu_0^N \equiv F(N,0) - F(N-1,0)$,

$$\kappa = \beta \frac{\frac{g(N)}{g(N-1)} e^{\beta(\delta\mu - \Delta F)}}{\left(1 + \frac{g(N)}{g(N-1)} e^{\beta(\delta\mu - \Delta F)}\right)^2}, \tag{2.3}$$

where $\delta\mu = \mu - \mu_0^N$ and $\Delta F = F(N,T) - F(N-1,T) - \mu_0^N$. We differentiate with respect to $\delta\mu$ to find the centre of the peak: $\delta\mu_{\max} = T\ln\left(g(N-1)/g(N)\right) + \Delta F$. For a tightly confining circular well at low T, for which $\Delta F = 0$, this gives $\delta\mu_{\max} = \pm(T/2)\ln 2$, which confirms that the charging line slopes alternate sign as a function of the parity of N. In the intermediate regime, the slope is negative for all N. The peak height decreases with T as $\kappa_{\max} \sim 1/4T$, while the full-width-half-max (FWHM) increases with T due to number fluctuations as FWHM $\sim 2T\ln(3+2\sqrt{2})$, roughly ten times as fast as the shift in position. Nevertheless, tracing the peak should be possible if measurements are sufficiently accurate. In the experimental regime of interest, the charging energy $U(N) = \mu_0^N - \mu_0^{N-1} \gg T$, so the peaks remain distinguishable. The key input to the above statistical model is the microcanonical low-energy spectra of fixed numbers of QPs in a well, which we now calculate for $N = 1, 2$.

2.6 One Particle

For a particle in an elliptical harmonic well,

$$V_{\text{trap}} = \frac{1}{2}k\left(x^2 + \alpha y^2\right), \tag{2.4}$$

where k is the spring constant, and α controls the eccentricity ($\alpha = 1$ defines a circular trap), the level-spacing is $\Delta_1 = k\sqrt{\alpha}{l_B^*}^2$, where $l_B^* = \sqrt{\hbar/e^*B}$ is the effective magnetic length for QPs in a magnetic field B. At finite T, this produces an internal free energy,

$$F(1,T) = T\ln(1 - e^{-\Delta_1/T}). \tag{2.5}$$

This free energy decreases weakly with T for $T < \Delta_1$, only significantly correcting the linear charging curve for $T \gg \Delta_1$, as shown in figure 2.1.

2.7 Two Particles

As the fusion channel, f, of two orbiting non-Abelian anyons is conserved, the orbital dynamics may be treated separately in each f-sector. This reduces to the dynamics of Abelian anyons whose statistical angle θ depends on the fusion sector. For Ising anyons, $\theta_1 = 0$ and $\theta_\psi = \pi/2$ [13]. To model two such anyons in a well, each with charge $e^* = e/4$, we write the Hamiltonian for a pair of Bosons with a statistical gauge field:

$$\begin{aligned} H =& \frac{1}{2m}\sum_{i=1}^{2}\left(\vec{p}_i - \hbar\vec{a}_i^f - e^*\vec{A}_i\right)^2 + V_{\text{trap}}(\vec{r}_i) + \\ &+ V_I(\vec{r}_1 - \vec{r}_2) + V_X^f(\vec{r}_1 - \vec{r}_2). \end{aligned} \tag{2.6}$$

The first term contains the electromagnetic vector potential $\vec{A}_i$, corresponding to a uniform external B-field, as well as a statistical gauge field $\left(a_x^f, a_y^f\right) = \frac{\theta_f}{\pi r^2}(y, -x)$, which binds a flux tube of strength θ_f to each quasiparticle, and m is the effective QP mass. We project into the LLL, taking $m \to 0$. The coordinates in $\vec{a}_i$ are relative to the other particle. We assume that the QPs interact via a Coulomb interaction, $V_I = \frac{e^{*2}}{4\pi\epsilon r}$, where $\epsilon \equiv \epsilon_r\epsilon_0$ is the electric permittivity of the material. This approximation is valid assuming that QPs do not come within l_B^* of each other. V_X is the direct energy splitting of the fusion channels due to virtual exchange of Majorana Fermions. It is related to the fusion channel splitting discussed in [55, 56], and should consist of an exponential decay and oscillations, each on the order of several l_B^*. For

circular wells, the behaviour of Abelian anyons has been treated previously [61–64]. We summarise key results, and include corrections due to eccentricity.

In the symmetric gauge for harmonic traps, the centre-of-mass (CM) and relative (REL) coordinates decouple. In the CM coordinate, the statistical gauge field $\vec{a}^f$ falls out, leaving a single particle projected into the LLL in a harmonic well. For the REL coordinate, the particle is confined to a half-plane with the origin removed, and $\vec{a}^f$ remains [62]. We change the gauge, so that $\vec{a}^f = 0$, giving a twisted boundary condition, $\psi_{REL}(r,\pi) = e^{i\theta_f}\psi_{REL}(r,0)$. The potential landscape in the half-plane is defined by strong Coulomb repulsion near the origin together with the harmonic trap, $V_{\text{trap}} + V_I$, for $V_X = 0$. The twisted periodic boundary conditions allow only angular momenta $\ell = 2n + \theta/\pi$, for n integer. The REL-coordinate wave-functions in the LLL have a basis given by $|\ell\rangle$,

$$\langle z|\ell\rangle = N_\ell^{-\frac{1}{2}} z^\ell e^{-|z|^2/4(2{l_B^*}^2)}, \tag{2.7}$$

where $z = x + iy$ and N_ℓ is a normalisation constant on the half-plane. In this basis, we can diagonalise to find the two-particle spectrum. The potential has diagonal terms, as well as an off-diagonal term only when circular symmetry is broken.

2.8 Circular Well

We assume $V_X = 0$ initially, and note that the CM coordinate behaves just like the single particle case with $\Delta_{\text{CM}} = \Delta_1$. The lowest energy gap Δ_{R}^f in the relative coordinate within a fusion channel f can be found by taking differences between adjacent ℓ-states near the minimum, obtained by diagonalising the Hamiltonian. We

define the parameter $r_0 = (e^{*2}/2\pi\epsilon k)^{1/3}$, the radial position of the minimum of the potential. This splitting Δ_{R}^f oscillates with r_0 at fixed magnetic field with an amplitude that decays in the large-well limit, $r_0 \gg l_B^*$, as

$$\Delta_{\mathrm{R}}^f \lesssim 12\Delta_1 \frac{r_0^2}{l_B^{*\,2}} = 24\frac{e^{*2}}{4\pi\epsilon}\frac{l_B^{*\,4}}{r_0^5}, \tag{2.8}$$

The other relevant gap for the relative coordinate is the energy difference $E_{1\psi} = |E_0^1 - E_0^\psi|$ between lowest energy states in the 1 and ψ channels. With $V_X = 0$, the splitting between fusion channels is an interchange effect, which follows from the allowed angular momenta in each channel; in particular, $E_{1\psi}$ behaves similarly to Δ_{R}^f with a maximum oscillation bounded by the power law $\frac{9}{2}\frac{e^{*2}}{4\pi\epsilon}\frac{l_B^{*\,4}}{r_0^5}$, which is approximately 20% of the amplitude of Δ_{R}^f. For $T < E_{1\psi}$ and Δ_{R}^f, the slope of the 1-2 transition in the $\mu - T$ plane is positive, exhibiting the even-odd effect. Clearly, intra-channel entropy washes out the effect for $T > \Delta_{\mathrm{R}}^f$. As r_0 varies, $E_{1\psi}$ will oscillate in sign, and can be arbitrarily small if r_0 is close to a zero-crossing. If $E_{1\psi} < T < \Delta_{\mathrm{R}}^f$, the 0-1 and 1-2 charging lines are parallel with negative slope $-2/\ln 2$.

Non-Abelian QPs at finite separation can exchange Majorana Fermions, leading to an additional fusion channel splitting. Unlike the orbital contribution, this splitting occurs even when QPs are localised. Using a variational method to calculate this energy splitting for particles on a sphere, it was found to decay exponentially on the order of several magnetic lengths, up to a numerical pre-factor of $\mathcal{O}(1)$ [56]. V_X in the Hamiltonian accounts for a splitting of this form. We do not calculate V_X explicitly, but note that while it dominates the shift between fusion channel spectra in tightly confining wells, it oscillates and decays exponentially as the well widens and particle separation increases. In general, V_X increases $E_{1\psi}$, promoting the even-odd effect

over a larger T-range, and making a regime of parallel charging lines less likely.

2.9 Anisotropic Well

For anisotropic wells, again taking $V_X = 0$ initially, consider the relative coordinate for two QPs. Starting from the circular well where QP orbits encircle the origin in the half-plane, as the eccentricity α increases, the effective potential acquires a minimum on the x-axis, at $x = r_0$, and a saddle point on the y axis at $y = r_0/\alpha^{1/3}$. For any given $\alpha > 1$, the wavefunction becomes effectively localised near the potential minimum for $(r_0/l_B^*)^2 > \frac{2}{\sqrt{3}} \frac{\sqrt{\alpha-1}}{(\alpha^{1/3}-1)} \equiv \lambda(\alpha)$. This is when the lowest-energy state near the minimum has energy lower than the saddle point potential. As $\alpha \to 1$, $\lambda(\alpha)$ diverges as $(\alpha - 1)^{-1/2}$, confirming that for a circular well, QPs are not localised. Eccentricity breaks any accidental degeneracies which arise in the circular potential near r_0, and modifies the spectrum of the well. For low eccentricities, the degeneracy breaking can increase or decrease the orbital splitting. For large enough α, the QPs are trapped at opposite ends of the well, and no longer orbit each other, except for quantum tunneling across the saddle point. In a saddle point tunneling model, the orbital exchange rate, R, in the large well limit is Gaussian in the well-size, $R \approx k{l_B^*}^2 \exp[-\alpha^{-1/2}\lambda(\alpha)^{-1} c(\alpha) \, (r_0/l_B^*)^2]$, where $c(\alpha)$ depends weakly on α and goes to a constant of order unity as $\alpha \to 1$. This expression may be obtained by estimating the potential as Harmonic near the minimum, and using a WKB type calculation of the tunneling of a particle near a quadratic saddle point in the LLL, as in [65]. Increasing α also has the effect of raising the energy of the ground state, by increasing the harmonic frequency of the trap.

For anisotropic wells with $V_X \neq 0$, the exchange effect naturally dominates the splitting at large r_0, since the exchange of neutral Majorana Fermions decays exponentially while the interchange of localised charged particles in a magnetic field decays as a Gaussian. We recover the even-odd effect for T below this splitting, regardless of QP localisation.

2.10 Energy Estimates

A simple model producing a charge trap is provided by considering a point-like gate, a distance d above the 2DEG. A charge $+|e|$ on this gate produces an effective circular harmonic trap in the plane with spring constant $k = \frac{|ee^*|}{4\pi\epsilon d^3}$. Using $\epsilon_r = 13$ for GaAs/AlGaAs quantum wells, $B = 3.5$T and $d = 100$nm, we find $r_0 = 63$nm. The charging energy is 1.6K, and the gap to single particle excited states in the well is $\Delta_1 \approx 0.24$K, preserving the slope of $-2/\ln 2$ throughout the accessible experimental range $20\text{mK} \lesssim T \lesssim 80\text{mK}$. The 1-channel ground state has lower energy than the ψ-channel by $E_{1\psi} \approx 29$mK in the absence of V_X, and the intrachannel gap $\Delta^1_{\mathrm{R}} \approx 220$mK, above the accessible range. As $r_0/l^*_B \approx 2.3$, we expect the contribution of V_X to enhance the even-odd effect. Since the calculated charging energy is larger than the energy gap for the $\nu = 5/2$ plateau, it is probably impossible to observe multiple transitions in a single well simply by changing the voltage on a back gate. However, applying a voltage to a point-like gate on top of the sample can change the depth of a well by a large amount without inducing QPs in the surrounding 5/2 state.

To further enhance the even-odd effect, all energy gaps need to be increased. Increasing the charge on a point-gate or reducing the setback distance d makes the

confining trap tighter. Increasing the magnetic length – by lowering B while maintaining the filling fraction – increases all of the relevant splittings in a fixed trap geometry.

2.11 Matrix Elements

The normalisation constant is:

$$\begin{aligned}\langle \ell|\ell\rangle &= \frac{1}{N_\ell}\int_0^\infty r dr \int_0^\pi d\phi \left(\frac{r}{l_B}\right)^{2l} e^{-r^2/4l_B^2} \stackrel{!}{=} 1 \\ \Rightarrow N_\ell &= \pi 2^\ell l_B^2 \Gamma\left(\ell+1\right),\end{aligned}$$

where $\Gamma(x)$ is the gamma function. The basis states are proportional to $e^{-r^2/8l_B^2}$ as opposed to the usual $e^{-r^2/4l_B^2}$ because r is the relative coordinate. The potential has diagonal terms, as well as an off-diagonal term only when circular symmetry is broken ($\alpha \neq 1$):

$$\begin{aligned}\langle \ell|\, V_{\text{trap}}^{REL}\, |\ell\rangle &= \frac{(1+\alpha)}{2} k {l_B^*}^2 (\ell+1) \\ \langle \ell|\, V_{\text{trap}}^{REL}\, |\ell+2\rangle &= \frac{(1-\alpha)}{4} {l_B^*}^2 k \sqrt{(\ell+2)(\ell+1)} \\ \langle \ell|\, V_I\, |\ell\rangle &= \frac{e^{*2}}{8\pi\epsilon l_B^*}\frac{\Gamma[\ell+1/2]}{\Gamma[\ell+1]}.\end{aligned} \tag{2.9}$$

Note that integration is over the half-plane, since we are working in the relative coordinate. The fusion-channel dependence is hidden in $\ell = 2n + \theta_f/\pi$. For $\theta = 0$ (π) the results apply to Bosons (Fermions).

2.12 Saddle Point

We demonstrate how to obtain the tunneling rate through a saddle point stated in section 2.9. In the REL coordinate for two particles, the potential is:

$$V(r) = \frac{\zeta}{r} + \frac{1}{2}\left(\frac{k}{2}\right)\left(x^2 + \alpha y^2\right), \tag{2.10}$$

with $\zeta = e^{*2}/4\pi\epsilon$ and effective magnetic length $\sqrt{2}l_B^*$. In the circular case, $\alpha = 1$, the minimum is circularly symmetric at $r_0 = (2\zeta/k)^{1/3}$. For $\alpha \neq 1$, in the x-y plane, $(r_0, 0)$ is still a minimum, and $(0, r_s)$ is a saddle point, with $r_s = r_0/(\alpha^{1/3})$. Expanding to quadratic order near the minimum and the saddle point gives:

$$\begin{aligned} V(x - r_0, y) &= V(r_0) + \frac{1}{2}\frac{3k}{2}\left[\delta x^2 + \left(\frac{\alpha}{3} - \frac{1}{3}\right)\delta y^2\right], \\ V(0, y - r_s) &= V(r_s) + \frac{1}{2}\frac{3k\alpha}{2}\left[\left(\frac{1}{3\alpha} - \frac{1}{3}\right)\delta x^2 + \delta y^2\right], \end{aligned} \tag{2.11}$$

where as expected the transverse components vanish in the circular case, and the energy levels near r_0 are $E_n = V(r_0) + 3k{l_B^*}^2\sqrt{(\alpha-1)/3}(n + 1/2)$. We compare the ground state near r_0 to the height of the saddle point, $V(r_s)$, namely:

$$\delta E = V(r_s) - E_0 = \frac{3k}{2}\left[\frac{1}{2}r_0^2(\alpha^{1/3} - 1) - {l_B^*}^2\sqrt{\frac{\alpha - 1}{3}}\right]. \tag{2.12}$$

Solving for $\delta E > 0$ gives the condition $(r_0/l_B^*)^2 > \lambda(\alpha)$ described in section 2.9. To find the tunneling rate through the saddle point, we use the expression for the transmission through a saddle point potential $V_{SP}(x, y) = -U_x x^2 + U_y y^2$ given in [65], $T = (1 + \exp(-\pi E))^{-1}$, where $E = -\delta E/\epsilon_1$, $\epsilon_1 = \sqrt{U_x U_y}/m\omega_c$ in the large B-limit, and ω_c is the cyclotron frequency. For the saddle point under consideration, $m\omega_c = 1/2{l_B^*}^2$, and $\epsilon_1 = \frac{k}{2}\sqrt{3\alpha(\alpha-1)}{l_B^*}^2$, giving:

$$E = \frac{-3\left[\frac{1}{2}r_0^2(\alpha^{1/3} - 1) - {l_B^*}^2\sqrt{\frac{\alpha-1}{3}}\right]}{\sqrt{3\alpha(\alpha-1)}{l_B^*}^2}, \tag{2.13}$$

which reduces to $E \sim \frac{-1}{2\sqrt{3\alpha}} \left(\frac{r_0}{l_B^*}\right)^2 \frac{\alpha^{1/3}-1}{\sqrt{\alpha-1}}$ for large r_0/l_B^*, and in this limit, $T \sim \exp(\pi E)$. To convert from transmission probability to a transmission rate, we take the velocity of a QP about its orbit as the ratio of the gradient of the potential to the magnetic field, and dividing by the circumference of an orbit near the minimum, we find the frequency of the orbit is $\sim k{l_B^*}^2$, which, multiplied by T, gives the rate R reported in section 2.9.

2.13 2-particle Splittings

The maximum values for the gaps Δ^f and $E_{1\psi}$ in the two-particle REL spectrum are given in section 2.8. The pre-factors are found by expanding the potential near the minimum at r_0, finding the lowest-energy and first excited states in terms of allowed angular momenta, and expanding terms as a function of $l_B^*/r_0 \ll 1$. To find the angular momentum corresponding to the lowest energy state, we use the relation $r = \sqrt{2\ell} l_B^*$ to find ℓ_0, the (possibly not allowed) angular momentum corresponding to r_0, we first find the allowed angular momenta right above and below:

$$\ell_- = 2\lfloor(\ell - \theta_f/\pi)/2\rfloor + \theta_f/\pi \tag{2.14}$$

$$\ell_+ = 2(\lfloor(\ell - \theta_f/\pi)/2\rfloor + 1) + \theta_f/\pi, \tag{2.15}$$

where $\lfloor\cdot\rfloor$ is the integer floor function. Next, we convert back to positions corresponding to these momenta, and plug back into the potential to check which state has lower energy. If ℓ_g is the angular momentum of the ground state, then the angular momentum of the first excited state is $\ell_1 = \ell_g \pm 2$. This argument is sufficient for crudely extracting the large r_0 behaviour of the intra-channel gap Δ^f. A similar calculation

produces $E_{1\psi}$.

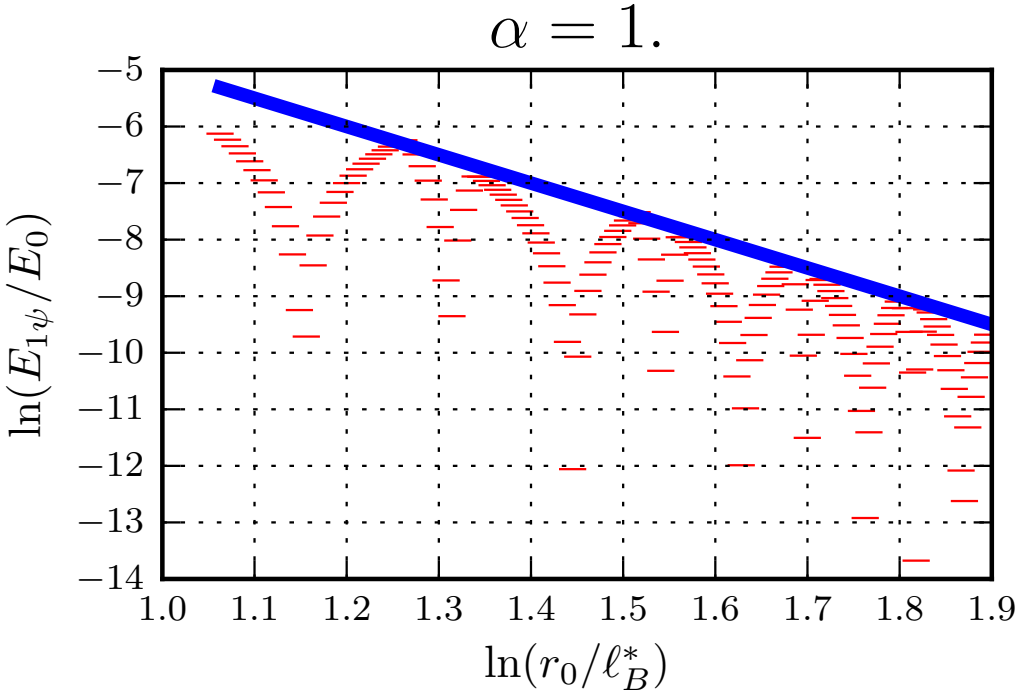

Figure 2.2: $\log(E_{1\psi}/E_0)$ calculated numerically by exact diagonalisation, vs. $\log(r_0/l_B^*)$ for a circular well. A power law r_0^{-5} is also plotted as a guide to the eye. $E_0 = \frac{9}{2}\frac{e^{*2}}{4\pi\epsilon}\frac{1}{l_B^*}$, as described in the paper below equation 8, with the r_0/l_B^* dependence factored out.

The decay of $E_{1\psi}$ is plotted in figure 2.2 for a circular well; the log-log plot demonstrates a power law decay as r_0^{-5}. Figure 2.3 shows the decay of $E_{1\psi}$ for an elliptical well with $\alpha = 1.3$; the quadratic decay in a log plot confirms a Gaussian form as expected from the saddle-point calculation.

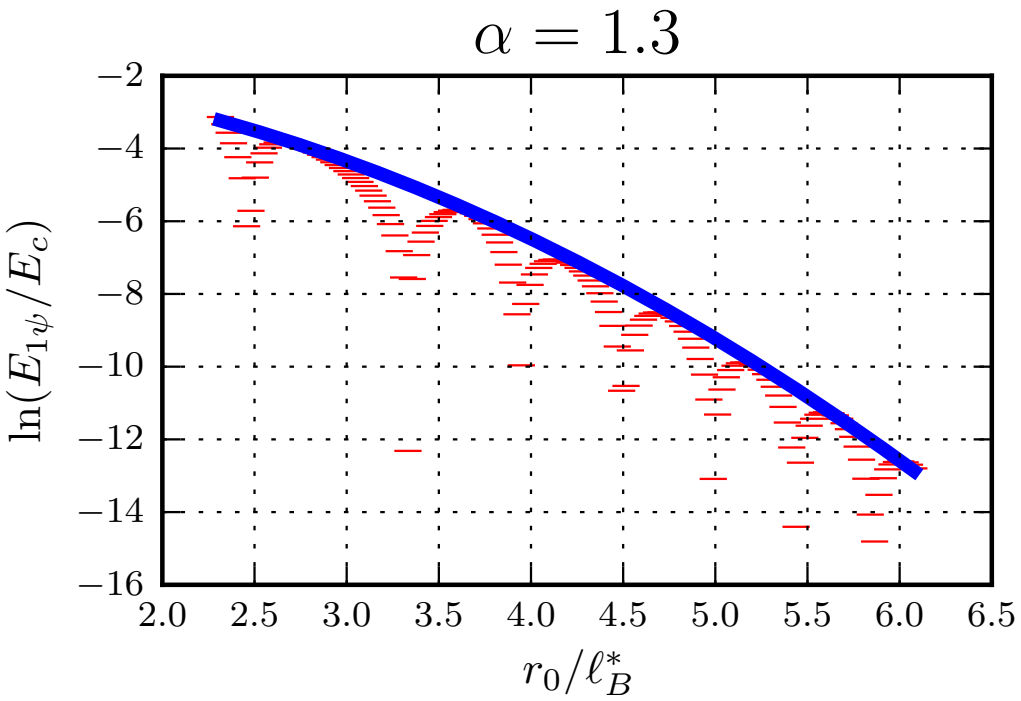

Figure 2.3: $\log(E_{1\psi}/E_c)$ calculated numerically by exact diagonalisation, vs. r_0/l_B^* for an elliptical well, with $\alpha = 1.3$. A Gaussian decay $\exp(-cr_0^2)$ is also plotted as a guide to the eye. $E_c = \frac{e^{*2}}{4\pi\epsilon}\frac{1}{l_B^*}$ is the Coulomb energy scale.

2.14 Relations between κ , the local incompressibility, and the SET signal.

2.14.1 Chemical Potential v. Backgate

In this chapter, we calculate κ, the change in local average number of QPs as a function of the local chemical potential of the QPs. Charge stability diagrams are then drawn as a function of the QP chemical potential. The proposed SET measurements reveal the *inverse compressibility* by measuring the change of the local electrostatic potential in the 2DEG as a function of a global backgate voltage. The electrostatic potential is then converted to chemical potential of electrons, under the assumption that electrochemical potential is held constant. A capacitance model is used to convert backgate voltage to average electron density. The qualitative even-odd effect is independent of definitions, but the quantitative slope predicted needs to be scaled to match experimental parameters.

2.14.2 Relation of the SET signal to the local incompressibility

We elaborate here on the relation between the local quasiparticle compressibility, discussed in this paper, and the signal measured in an SET experiment, which is commonly described as measuring the local electronic *incompressibility*. Throughout the remainder of this chapter, we consider a sample with its top surface at $z = 0$. A 2DEG is found a distance d below the surface, and a backgate is placed a distance D below the 2DEG, at $z = -(d + D)$. The SET will be placed just above the sample surface, $z = 0^+$.

A more precise description of the SET signal is that it measures $\partial\Phi_{\rm SET}/\partial V_G$, where $\Phi_{\rm SET}$ is the electrostatic potential at the SET, and V_G is the back-gate voltage. In this measurement, the electrochemical potential of the 2DEG is held fixed at a voltage V, by connecting it to a metallic lead. (In ref [23], the lead is grounded; i.e., the 2DEG is in equilibrium with a ground surface at infinity, and we may take $V = 0$.) Furthermore,

$$\delta\Phi_{\rm SET} = \int d^2\vec{r}\, K(\vec{r} - \vec{r}_0)\, \delta\Phi(\vec{r}),$$

where $\Phi(\vec{r})$ is the electrostatic potential at a point $\vec{r}$ just above the plane of the 2DEG, inside the GaAs, $\vec{r}_0$ denotes the horizontal location of the SET probe, and the precise form of the kernel K depends on the height of the SET probe above the semiconductor surface, the depth of the 2DEG, and dielectric constant ϵ of the material. In general, the fluctuation in $\Phi_{\rm SET}$ may be interpreted as a weighted spatial average of Φ within a distance of the order of the SET-2DEG separation, d.

It is customary to define a local chemical potential for electrons in the 2DEG, by

$$\mu_e(\vec{r}) \equiv e[V - \Phi(\vec{r})],$$

where $e < 0$ is the electron charge. The change in the average density of electrons in the 2DEG produced by a change in the back-gate voltage is

$$\delta\bar{n} = -C\delta V_G/e,$$

where C is an effective capacitance per unit area. Then, if we define the local electronic incompressibility by $\gamma(\vec{r}) \equiv \partial\mu_e(\vec{r})/\partial\bar{n}$, we see that

$$\frac{\partial\Phi_{\rm SET}}{\partial V_G} = \frac{C}{e^2}\int d^2\vec{r}\, K(\vec{r} - \vec{r}_0)\, \gamma(\vec{r}),$$

Moreover, if we define $\bar{\gamma}$ as the spatial average of the local incompressibility $\gamma(\vec{r})$, one finds

$$C^{-1} = \frac{D}{\epsilon} + \frac{\bar{\gamma}}{e^2},$$

where D is the distance to the back gate. We note that $\bar{\gamma}$ will be finite, even when the bulk of the system sits in the quantum Hall plateau, due to the effects of changing quasiparticle populations in wells whose depths are close to a critical value. In practice, in the experimental geometry where D is the order of a micrometer, the first term will be large compared to the second, and C will be determined primarily by the geometric capacitance.

2.14.3 Relation between the SET signal and the local quasiparticle compressibility

As a consequence of Poisson's equation, the value of $\Phi(\vec{r})$ will be directly affected by changes in the local electron density $n(\vec{r})$. In the simplest case, we consider a situation where there is a single chargeable potential well, surrounded by a region of incompressible 5/2 state, in the area sensed by the SET. Then changes in the local electron density result primarily from changes in N, the quasiparticle occupation number of the well. To a good approximation,

$$\frac{\partial \Phi_{\mathrm{SET}}}{\partial V_G} \approx \eta(d) \frac{\delta N}{\delta V_G} + c_1,$$

where η is the model-dependent potential at the SET from a single QP, and c_1 is a slowly varying number accounting for the change in density in the rest of the sample beyond the well.

The quasiparticle chemical potential μ employed in our paper is related in a complicated way to the local electron chemical potential μ_e. Roughly,

$$\delta\mu = -e^*\delta\tilde{\Phi}$$

where $\tilde{\Phi}$ is the electrostatic potential at the position of the well, *excluding any potential due to the presence of one or more quasiparticles in the well.* When the expectation value of N is a rapidly varying quantity, there will be a very large difference between the variation in $\tilde{\Phi}$ and the variation in $\Phi(\vec{r})$.

In general, we expect that $\tilde{\Phi}$ should depend smoothly on the back-gate voltage V_G. We may estimate this dependence by assuming that the potential well is surrounded by an incompressible region of radius R, and that outside this region we have a continuous medium characterized by a finite incompressibility $\bar{\gamma}$, which we identify with the spatial average of $\gamma(\vec{r})$ defined above. We shall assume that D is very large compared to R and to the "screening length" $l_s \equiv \bar{\gamma}\epsilon/e^2$, but we should still consider different values of the ratio R/l_s. In the case $R > l_s$, analysis of the resulting electrostatics problem leads to a result

$$\delta\tilde{\Phi} \sim c_2\delta V_G\, R/D$$

where c_2 is a constant of order unity. In the opposite limit, $l_s > R$, we find

$$\delta\tilde{\Phi} \sim \delta V_g l_s/D = \delta V_G\bar{\gamma}/Ce^2.$$

When the system is in the middle of a quantum Hall plateau, we expect that $\bar{\gamma}$ will be large, and we might expect to be in the regime $l_s > R$.

Finally we may put these results together to find the relation between the SET signal and the quasiparticle compressibility. In the limit where $l_s > R$, we have,

ignoring a smooth background contribution,

$$\frac{\partial \Phi_{\mathrm{SET}}}{\partial V_G} \approx -\left(\frac{e^*}{e}\right)^2 \frac{\epsilon\,\bar{\gamma}\,\kappa}{D}\frac{\eta(d)}{e^*}.$$

The above model can be generalized to a situation where there are several wells beneath the SET tip, by choosing a larger radius R within which there is no continuum background compressibility, and including explicitly the Coulomb interactions between quasiparticles in different wells in this region. In the simpler model we have replaced all wells by a continuum, except for the one under consideration.

2.14.4 Calculation of $\eta(d)$

We calculate $\eta(d)$ for a point-like SET, located an infinitesimal distance above the sample surface, which is a distance d from the 2DEG. The distance to the back-gate, D is taken to be much larger than d. We consider a QP of charge e^* added to the 2DEG in a bulk sample with permittivity ϵ, and we want to know the potential at the SET, when the sample sits in vacuum - i.e outside, permittivity is ϵ_0. We have to solve the following equations for an electric field $\vec{E}$:

$$\epsilon\vec{\nabla}\cdot\vec{E} = \rho, \quad z<0$$

$$\epsilon_0\vec{\nabla}\cdot\vec{E} = 0, \quad z>0$$

$$\vec{\nabla}\times\vec{E} = 0, \quad \text{everywhere},$$

with boundary conditions at the sample boundary (i.e. $z=0$) of continuous $\vec{E}$-fields in the x and y directions, and $\lim_{z\to 0^+}\epsilon_0 E_z = \lim_{z\to 0^-}\epsilon E_z$. Place an image charge q' at $z=d$ above the surface, and then using cylindrical coordinates (r,ϕ,z), the potential

at any point inside the sample is:

$$\phi = \frac{1}{\pi\epsilon}\left(\frac{e^*}{R_1} + \frac{q'}{R_2}\right), \quad z < 0, \tag{2.16}$$

where $R_1 = \sqrt{r^2 + (d+z)^2}$, $R_2 = \sqrt{r^2 + (d-z)^2}$. For the region $z > 0$, which is where the SET is, there are no charges, and the potential must therefore be a solution to Laplace's equation without singularities. The simplest solution is the potential from an effective charge q located at the site of the QP e^*, giving a potential:

$$\phi = \frac{1}{4\pi\epsilon_0}\frac{q}{R_1}, \quad z > 0. \tag{2.17}$$

The solutions 2.16 and 2.17 can be matched at $z = 0$ and must satisfy the boundary conditions, giving $e^* - q' = q$ and $(e^* + q')/\epsilon = q/\epsilon_0$. This implies $q = (2\epsilon_0/\epsilon + \epsilon_0)\, e^*$. We thus find the potential at the SET due to the QP to be:

$$\eta(d) = \frac{1}{4\pi}\frac{2}{\epsilon + \epsilon_0}\frac{e^*}{d}.$$

A very similar calculation can be found in section 4.4 in [66].

2.15 Conclusion

The detection of non-Abelian QPs through local charge-sensing measurements falls within realistic experimental parameters. A sensitive compressibility measurement could extract slopes reflecting the degeneracies of the ground state. Additional control over confinement potentials will allow for even more conclusive experiments.

Chapter 3

Detecting Majoranas in 1D wires by charge sensing

3.1 Overview

The electron number-parity of the ground state of a semiconductor narowire proximity-coupled to a bulk superconductor can alternate between the quantised values ± 1 if parameters such as the wire length L, the chemical potential μ or the magnetic field B are varied inside the topological superconductor phase. The parity jumps, which may be interpreted as changes in the occupancy of the Fermion state formed from the pair of Majorana modes at opposite ends of the wire, are accompanied by jumps δN in the charge of the nanowire, whose values decrease exponentially with the wire length. We study theoretically the dependence of δN on system parameters, and compare the locations in the μ-B plane of parity jumps when the nanowire is or is not proximity-coupled to a bulk superconductor. We show that, despite the fact

that the wave functions of the Majorana modes are localised near the two ends of the wire, the charge-density jumps have spatial distributions that are essentially uniform along the wire length, being proportional to the product of the two Majorana wave functions. We explain how charge measurements, say by an external single-electron transistor, could reveal these effects. Whereas existing experimental methods require direct contact to the wire for tunneling measurements, charge sensing avoids this issue and provides an orthogonal measurement to confirm recent experimental developments. Furthermore, by comparing density of states measurements which show Majorana features at the wire ends with the uniformly-distributed charge measurements, one can rule out alternative explanations for earlier results. We shed light on a new parameter regime for these wire-superconductor hybrid systems, and propose a related experiment to measure spin density.

3.2 Introduction

The isolation of zero-energy Majorana modes is an essential step in various proposals to perform topologically protected quantum computation [5]. The existence of localised Majorana modes has been predicted in several condensed matter systems, although definitive detection of such modes remains an open challenge [12, 27, 67–72], and in cold atom systems [73].

A promising physical system for realizing these modes consists of a one-dimensional (1D) semiconductor wire with strong Rashba spin-orbit coupling, coupled to a bulk s-wave superconductor (SC), and with a strong applied magnetic field [28, 29]. Under appropriate conditions, this system can enter a “topological" state, which would

exhibit isolated Majorana Fermions at the wire ends. The condition for a wire with strong spin-orbit interaction to enter this topological regime, is $E_Z^2 > \Delta^2 + \mu^2$, where E_Z is the Zeeman energy, proportional to the applied magnetic field B, while Δ is the induced superconducting pair potential in the wire, and μ is the chemical potential of the wire, measured relative to the electron energy at wave vector $k = 0$ when $E_Z = \Delta = 0$.

For an infinitely long wire in the topological regime, the wire has two possible ground states which are perfectly degenerate. The Majorana modes appear at the ends of the wire as zero-energy mid-gap states in the Bogoliubov-deGennes (BdG) spectrum. Moreover, in this limit the charge density distribution is precisely the same in the two ground states. For a long but finite wire, the two lowest-energy states of the wire will generally not be perfectly degenerate, but will be split by a small amount, which decreases exponentially as the wire becomes long. Similarly, the charge density distributions in the two states will differ by a small amount.

Since Fermion number is conserved mod 2 in the Hamiltonian of the system, the number parity is a good quantum number, which differs in the two competing ground states. We can classify the parity by the eigenvalue of the number parity operator, ± 1, and we call these even/odd respectively. If parameters such as B or μ or the length L of the system are varied, the energies of the even and odd-parity states can cross, so the parity of the true ground state can jump discretely between even and odd.

Since the total charge on the nanowire is not conserved, it is not a good quantum number, and its expectation value, in general, will not be an integer as the ground

state will be a superposition of components with different electron number. For a finite wire, there will be a small but non-zero jump in the total electron number, whenever the parity changes, but the size of the jump can be much less than one electron charge. Between these jumps, the average number of electrons will vary continuously with the system parameters.

Although the quantum operators for Majorana modes do not obey the commutation relations of a normal Dirac Fermion creation or annihilation operator, one can construct a proper annihilation operator from a linear combination of the two Majorana operators at opposite ends of the wire. Following a BdG description, the difference between the even and odd parity many-body ground states is equivalent to whether the Fermion state corresponding to this annihilation operator is occupied or not. Moreover, the energy difference between the two ground state energies is just the BdG energy of this single Fermion state. Since eigenstates of the BdG equation occur in pairs with energies that differ by a sign, we may say that the degenerate zero-energy state is split in the finite wire, into states of positive and negative energy, due to a small overlap between the Majorana wave functions localised at the two ends. Jumps in the parity of the ground state occur when this energy splitting passes through zero. The charge difference between the even and odd parity ground states is equal to the net charge carried by the BdG Fermion state, which can be non-zero when the constituent Majorana wave functions overlap.

The purpose of this chapter is to explore in some detail the regions in the phase diagrams where parity jumps are expected, as well as the size of the jumps in electron charge expected at these transitions. We also compute the spatial distribution of

the jumps in charge density. Although the Majorana wave functions, and hence the tunneling density of states, are peaked at the wire ends, we show that the discontinuity in charge density arising from the overlap of the Majorana wave functions is spread essentially uniformly along the wire. Changes in total charge and charge density can be measured experimentally using charge sensing techniques.

We note that the number parity of the nanowire can change when a parameter is varied on laboratory time scales, even though the model Hamiltonian conserves parity, even in the absence of coupling to a normal lead. This is due to the presence of a small number of thermally activated quasiparticles in the bulk superconductor. These can be excited across the gap of the SC, or might result form hopping between localised states within the bulk SC.

In an important portion of the topological regime (see Sec. 3.4 below), it is predicted that the energy splitting of the Majorana modes will vary as $\delta E \sim \exp(-L/\xi)\cos(k_{\mathrm{F}}L)$, where ξ is the induced superconducting coherence length, k_{F} the Fermi wavevector, and L the length of the wire [74, 75]. Theoretically, the easiest way to probe this oscillatory splitting might be to vary L, bringing the ends closer together. In practice, however, the wire has a fixed length. It can be effectively shortened in discrete steps by depleting pieces of it using external gates, but local gating may lead to other unforeseen consequences.

Alternatively, an experiment can vary k_{F} to access the oscillations, and ξ to exhibit the exponential envelope. Both k_{F} and ξ depend on the chemical potential, which can be controlled with a global backgate, and on the applied external magnetic field. It has therefore been suggested in [74] to look for signatures of this dependence.

We demonstrate that charge-sensing measurements could reveal such oscillations, and thus may be a natural next step in the search for experimental verification of the elusive Majorana end modes.

Many recent experiments [30–36] have probed these one-dimensional semiconductor-superconductor hybrid systems by studying electron transport through the nanowire. Such transport experiments are very promising, but other physical mechanisms have been offered as explanations for the observed effects [76–81]. In particular, end effects, including Kondo physics [82], can cause zero-bias peaks similar to the ones observed. The alternate explanations suggest that the transport measurements may be sensitive to other effects beyond the possible Majorana modes predicted to exist at the ends of the wire. Furthermore, recent studies suggest that contact with a normal metal lead reduces the induced pair potential in the wire [83].

An alternative experiment, using capacitive coupling to a wire buried in a semiconductor heterostructure and designed to measure the global density of states by harmonic generation from high-frequency electric excitation, was proposed in [84] and is the basis of ongoing experiments Still another experiment, examining two coupled nanowires in a microwave cavity, is presented in [85], while a technique using an oscillating electrode is discussed in [86], and a proposal to use a resistive lead for tunneling measurements appears in [87].

Lin *et. al.* [88] proposed an alternate experiment to probe the Majorana states by charge sensing using a single electron transistor (SET). As addressed above and assumed in our discussion, such a measurement does not require tunneling to a normal lead, which could avoid some of the complications encountered in previous experi-

ments. Although the authors of [88] present numerical calculations that illustrate the charge density jumps associated with Majorana states in various cases, we present here a more detailed analysis of these features.

While we employ a simplified model of the physical system, in which we neglect the Coulomb interactions between electrons in the nanowire, we believe that results presented hold for real systems, and the effect should be visible in a realistic experiment. We address the effects of interactions in section 3.9 below. Various regimes in parameter space are discussed. We also address how to extract relevant system parameters using this technique, demonstrating that this experimental technique has other applications beyond the intended goal of detecting split Majorana end states.

We stress that a scanning charge measurement showing the additional charge spread across the wire, combined with a scanning tunneling measurement, can rule out alternative explanations of end effects for the previously observed features of Majorana physics.

The rest of this chapter is structured as follows. In Sec. 3.3, we present the model and relevant parameters. We then discuss the spectrum and number parity of systems with and without induced superconductivity in Sec. 3.4. We address the charge of the wire in three sections, beginning with an analytic analysis of the split Majorana modes in Sec. 3.5, followed by a numerical calculation of the total change in charge in Sec. 3.6, and then a discussion of the spatial distribution of the charge along the wire in Sec. 3.7. We end with an analysis of jumps in spin density in Sec. 3.8, a discussion of the effects of electron-electron interactions and screening in Sec. 3.9, and an overview of future experiments in Sec. 3.10.

3.3 Modeling

We model the wire using a standard BdG Hamiltonian:

$$H_{\mathrm{BdG}} = \left(-\frac{\partial_x^2}{2m} - \mu(x)\right)\tau_z + E_{\mathrm{Z}}\sigma_z\tau_z + \\ + i\alpha\partial_x\sigma_y\tau_z + \Delta\sigma_y\tau_y \tag{3.1}$$

where α is the Rashba spin orbit parameter, and $E_{\mathrm{Z}} = -g\mu_B B/2$ is the Zeeman energy in an applied magnetic field B, with g-factor g, and μ_B the Bohr magneton [89]. We have chosen the pair potential, Δ, proximity induced from the superconductor, to be positive and real. If tunneling between the SC and nanowire is strong, Δ can approach Δ_{SC}, the gap of the bare SC, whereas if the tunneling is weak, Δ can be arbitrarily small. The τ_j and σ_j are Pauli matrices in particle-hole and spin space respectively. We choose $\mu(x) = \mu$ constant along the length of the wire.

We find the eigenvalues, ϵ^ν, and the corresponding eigenfunctions,

$$\psi^\nu(x) \equiv \left(u^\nu_\uparrow, u^\nu_\downarrow, v^\nu_\uparrow, v^\nu_\downarrow\right)^{\mathrm{T}}. \tag{3.2}$$

We can then compute the average charge density at each site at finite temperature, with $f(\epsilon)$ the Fermi-Dirac distribution:

$$\langle\rho(x)\rangle_T = \sum_{\nu,\sigma} |u^\nu_\sigma(x)|^2 f(\epsilon^\nu) + |v^\nu_\sigma(x)|^2 f(-\epsilon^\nu), \tag{3.3}$$

where the sum is over states with $\epsilon^\nu > 0$. We can tune B and μ, and calculate the induced change of the charge.

To apply our model numerically, we rewrite the Hamiltonian on a 1D lattice with total length 2μm. For Figs. 1-3, we use 80 sites, and for Fig. 4 we use 160 sites.

Both give a band-width larger than all other energy scales, as desired for numerical accuracy. The figures shown in this chapter were computed using realistic parameters that might be appropriate for an InSb wire such as in the experiments in reference [30], namely: $\Delta = 0.25\text{m}e\text{V}$, $\alpha = 0.2e\text{V}\text{Å}$, $g = 50$, $m = 0.013m_0$, where m_0 is the electron mass. For completeness, we also tested the model for the system parameters from the Weizmann experiment [31], but all figures were plotted with the parameters defined here.

3.4 Spectrum and Parity

We begin by examining the case of a wire without a superconductor, to gain intuition of what one should expect before adding the superconductor. The system we consider consists of a semiconducting nanowire with large Rashba spin orbit (SO) coupling sitting on an insulating substrate with a global back-gate below, as shown in Fig. 3.1a. The substrate is required to break inversion symmetry for Rashba SO, and the back-gate allows for control of the chemical potential. Notice that we have a wire sitting on an insulator with no other contacts, not to be confused with the case of a wire connected to a metal whose superconducting gap is reduced, say by a magnetic field. If we think of Δ in the wire as being dependent on Δ_{SC} of a superconductor and the tunneling between the wire and the superconductor, this is equivalent to taking the tunneling to zero while keeping Δ_{SC} fixed. We nonetheless refer to this case as $\Delta = 0$. Fig. 3.1c shows the spectrum for a wire without a superconductor as a function of magnetic field, calculated from Eq. 3.1. The spectrum is not gapped, and the discrete states crossing the Fermi level are due to the finite length of the isolated

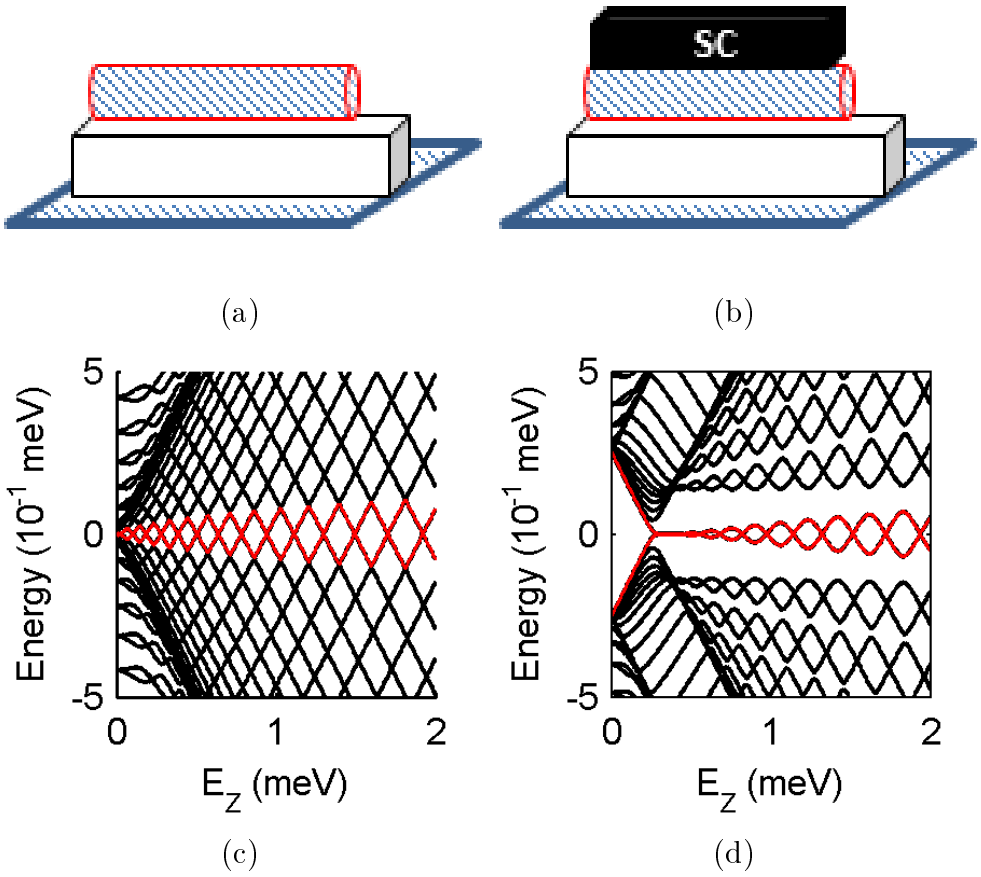

Figure 3.1: (a)/(b) Schematic of geometry. Semi-conducting nanowire sits on an insulating substrate (white), above a global backgate. Superconductor (in black) present in (b) but not (a). (c)/(d) Quasiparticle energy spectrum as function of Zeeman field E_Z for setups (a)/(b), with length $L = 2\mu$m, and other parameters $\mu = 0$, $\alpha = 0.2eV$, $m = 0.013m_0$, as defined in the text. Levels closest to zero are marked in red. In (c) we see discrete states from confinement. In (d), once in the topological regime $E_Z > \sqrt{\mu^2 + \Delta^2}$, we see the mid-gap degenerate Majorana states, which then split and oscillate (pair potential $\Delta = 0.25$meV).

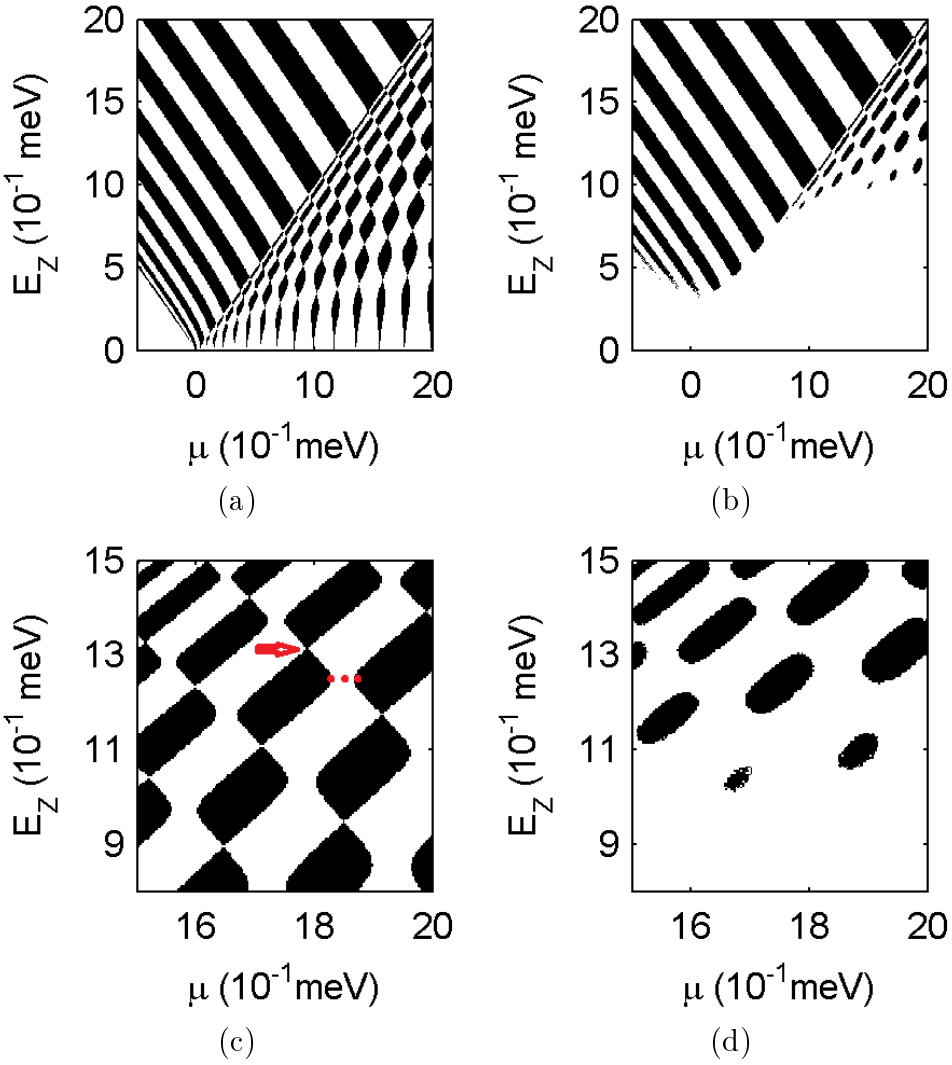

Figure 3.2: Electron-number parity of the system, for (a) wire without a superconductor to gain intuition, and (b) wire proximity coupled to a SC with a topological regime. (c)/(d) Zoom on upper-right part of (a)/(b). Arrow highlights a double degeneracy. Dotted line marks an avoided crossing. System parameters: $g = 50$, $\alpha = 0.8eV\text{Å}$, $L = 2\mu$m, $\Delta = 0$ in (a)/(c), and $\Delta = 0.25$meV in (b)/(d).

wire.

The number-parity of the wire is plotted as a function of μ and B, in Fig. 3.2a, with black regions corresponding to odd-parity states. In this case, the parity is calculated directly from the electron number in the wire, since it is well defined without superconductivity. The boundaries between regions of constant parity correspond to energy states crossing the Fermi level, as in Fig. 3.1c. These boundaries are the locus of points at which the system is compressible, and the charge changes discretely across these points as we fill each newly available state. We therefore refer to these parity plots as charging diagrams.

At $B = 0$, we see degenerate Kramer's pairs of opposite spin states, and thus no odd parity region. As we increase B these states are spin-split, and at high enough fields, all states at a given μ are spin-polarized. For intermediate B — i.e. $0 < E_{\mathrm{Z}} < \mu$ — we see figure-eight patterns in the charging diagram where states avoid each other at some values of μ and E_{Z} and cross at others. These can be seen more clearly in Fig. 3.2c, which focuses on a region of Fig. 3.2a. The avoided crossings (red dashed line in Fig. 3.2c) are due to spin-orbit coupling, and the degenerate points (red arrow in Fig. 3.2c) occur because the Rashba spin-orbit interaction only mixes opposite-spin states between wavefunctions with different spatial parity.

To see this, note that the Hamiltonian is a system of linear equations which mix the two spin species. Since, for $\Delta = 0$, H_{BdG} commutes with $P\sigma_z$, where P is the spatial inversion operator, it follows that states with different eigenvalues of $P\sigma_z$ have vanishing matrix elements. Equivalently, by writing the wave function for each spin expanded in Fourier modes, it is obvious that mixing of opposite spins occurs

only when the Fourier modes have opposite spatial parity. We calculate the spacing between avoided levels n and m, where level n is the n^{th} Kramer pair counting from $\mu = 0$, in a wire of length L. We find

$$\Delta E_{n,m} = \left| \frac{\alpha n m}{L(n^2 - m^2)} \right|, \tag{3.4}$$

where B is implicitly included in the equation since larger $|n - m|$ means states only approach each other at higher B. The avoided crossings can be used as another means to extract the value of α, the spin-orbit strength. Note that the spin-polarised states at high-B and the avoided-crossing figure-eights are the only two distinct regimes in this $\Delta = 0$ case.

Although it is not shown in the figures, we may also consider rotating the magnetic field from along the length of the wire, to the spin-orbit direction. When the applied B is parallel to the spin-orbit field, it is qualitatively equivalent to setting $\alpha = 0$, although α does provide a quantitative shift to the result. Indeed, the Zeeman split states no longer avoid each other, and just evolve linearly with B. We note that an experiment in which the magnetic field is rotated (see [90]) until the avoided crossings completely disappear provides a clear measurement of the spin-orbit direction. As discussed below, this can also be done for the wire-SC hybrid systems.

With these insights from the non-superconducting case, we consider a wire proximitised by a SC. This is similar to the above setup, although the wire is now coupled to a large superconductor, which we treat as a bath as in Fig. 3.1b. We assume that the wire and superconductor are in thermal equilibrium, such that Fermion parity can change on the time-scales of the experiment. In Fig. 3.1d, we show the spectrum for this case, under the same conditions as the non-superconducting case.

At low B, the system is gapped, and as a function of magnetic field the crossover from a non-topological state to a topological state is clear at $E_{\mathrm{Z}} = \sqrt{\Delta^2 + \mu^2}$ where the gap closes. Within the topological regime, we see the two mid-gap states oscillating, with energy crossings that correspond to parity changes of the wire. The splitting depends exponentially on the length of the wire, and goes approximately as $\exp(-L/\xi)\cos(k_F L)$, where ξ is the superconducting coherence length in the wire, and k_F the Fermi wave vector. Note that the splitting increases with increasing Zeeman field, since ξ increases with B [31, 74, 75].

We calculate the number parity in the wire with induced superconductivity, and plot it as a function of μ and B, in Fig. 3.2b. The method used to calculate the parity is discussed in section 3.11. The theoretical boundary between the topological and non-topological regimes corresponds to the curve

$$E_{\mathrm{Z}} = E_c \equiv \sqrt{\mu^2 + \Delta^2}, \tag{3.5}$$

and in the limit $L \to \infty$, the parity is constant below this curve. Below this boundary, the number of particles fluctuates as Cooper pairs are interchanged with the superconductor, but there are no changes in the parity. Within the topological regime, $E_{\mathrm{Z}} > E_c$, the mid-gap states have net spin polarisation and evolve linearly in the μ-B plane, similar to the wire without a superconductor. Between parity flips, the density varies continuously. Comparing the parity flips in Fig. 3.2b with the oscillations in the BdG spectrum – Fig. 3.1d – we see that the flips correspond precisely to the degeneracy points between the Majorana modes. This confirms that the parity flips are a signature of the split Majorana states crossing the Fermi energy.

We note that in an experiment, by fitting the outermost parity-flip, correspond-

ing to the topological boundary, to the hyperbola $E_Z = \sqrt{\Delta^2 + \mu^2}$ for small B and μ, the value of the induced pair potential Δ can be obtained. This is an important system parameter, whose value has an important effect on interpretation of experiments. Although Δ has been measured through transport measurements, independent confirmation is important, especially given the recent discussion of soft gaps due to leads [83]. However, this fitting procedure can be difficult, since at large B and μ, the topological boundary is only weakly dependent on Δ; we show an alternate way to extract Δ at the end of Sec. 3.6 below.

An interesting new parameter regime to examine is large B and μ, outside the topological region, i.e. $E_c > E_Z > \Delta$, the upper right side of Fig. 3.2b, and enlarged in Fig. 3.2d. Here we see parity flips, but they evolve quite differently from those within the topological region. In this non-topological regime, B is so strong that the wire is almost gapless, and the changes in parity are discrete and due to the finite length of the wire. At large enough B, this is true on both sides of the topological boundary. The figure-eight like patterns from the $\Delta = 0$ case are no longer present, as the double degeneracy points have now become avoided crossings.

For completeness, we may consider turning off the spin-orbit interaction, killing the mid-gap Majorana states. Setting $\alpha = 0$ in our model, one finds that the system has even parity for all μ and $E_Z < \Delta$. When $E_Z > E_c$, the alternating parallel parity stripes we saw in the other cases are present. For $\Delta < E_Z < E_c$, one finds a checkerboard pattern of constant parities formed by the two spin-states evolving in opposite directions with E_Z. Although this behaviour for $E_Z < E_c$ distinguishes the $\alpha = 0$ case from the $\alpha > 0$ case, we stress that both show very similar behaviour

when $E_Z > E_c$.

For a "topological" wire with $\Delta > 0$ and $\alpha > 0$, if the applied magnetic field is rotated so that it has a component along the direction of the spin-orbit-field, the system begins to behave as if it has no spin-orbit interaction ($\alpha = 0$). This is analogous to the avoided crossings disappearing when the field is rotated in the $\Delta = 0$ case, as discussed above. When this perpendicular magnetic field component becomes strong enough compared to the axial field, the charging diagram and the peak heights look like the $\alpha = 0$ case. The spin-orbit does not couple opposite spins, and just adds to the Zeeman field. It therefore no longer makes sense to discuss a topological regime. Rotating the field perpendicular to both the wire and the spin-orbit direction has no effect on the charging diagrams.

In all of the above discussion, the parity-transitions indicate that the system is compressible at these points in parameter space — it is possible to add charge. In particular, we can calculate the change in charge as we cross these boundaries. So far, it seems that in the three cases we have examined – the topological case, $\Delta = 0$, and $\alpha = 0$ – there are spin-polarised parity flips in the regime $E_Z > E_c$, each qualitatively indistinguishable from the other cases. In order to identify split Majorana Fermions, we need to distinguish between these three cases. To do so, we take a closer look at the size of the discrete charge jump across these parity-boundaries. This change in charge can be detected through compressibility measurements.

3.5 Jumps in charge density

In this section we show that while the Majorana wave functions are localised at the two ends of the wire, the jumps in the charge density are roughly uniform across the wire. We show that this happens because, roughly speaking, the difference in the charge density of the even and the odd ground states is given by $\delta\rho(x) = |u(x)|^2 - |v(x)|^2$ with $2u(x) = u_R(x) + iu_R(L-x)$ and $2v(x) = u_R(x) - iu_R(L-x)$, where $u_{R/L}(x)$ is an exponentially decaying (real) function peaked at the right/left end of the wire. One therefore obtains that $\delta\rho(x) = -u_R(x)u_R(L-x)$ is roughly uniform as the two exponential factors cancel each other. We derive here the expression for $\delta\rho(x)$ by calculating the full expression for the wave-functions $u(x)$ and $v(x)$.

Following the supplementary material of reference [74], we note that in the bulk of the wire, there are generally eight linearly independent solutions of the BdG differential equations at the energy $E = 0$. There are four solutions in which the spinor $u = \left(u_{|\uparrow\rangle}, u_{|\downarrow\rangle}\right)^T$ is pure real and in spinor notation, $v = u^* = u$, and four in which u is pure imaginary, and $v = u^* = -u$. The two classes are labeled, respectively by an index $\lambda = \pm 1$. The general solution for a fixed λ can be written as

$$u^\lambda(x) = \sum_{n=1}^{4} a_n e^{-z_n x} \rho_n, \tag{3.6}$$

where z_n are roots of the quartic equation

$$(\frac{z^2}{2m} + \mu^2)^2 - E_z^2 + (z\alpha - \lambda\Delta)^2 = 0, \tag{3.7}$$

and ρ_n are two component spinors, independent of x, whose explicit forms are given in reference [74].

For $\lambda = -1$, if the system parameters are in a topological superconductor phase, the quartic equation will have two complex conjugate solutions, denoted by $(z_1, z_2) = z_\pm$ which have positive real parts, one positive real solution, denoted $z_3 = w$, and one negative solution, which we denote $z_4 = s$. The spinors ρ_n may be chosen such that both components of ρ_3 and ρ_4 are real, while $\rho_1 = \rho_2^*$. Then, to obtain a solution with pure imaginary u_λ , we must choose a_3, a_4 to be pure imaginary, and $a_2 = -a_1^*$.

For $\lambda = 1$, the solutions of Eq (3.7) will be written as $z'_n = -z_n$, where z_n are the solutions for $\lambda = -1$ and the corresponding spinors are given by $\rho'_n = \rho_n$. In the non-topological phase, there will be two solutions with positive real parts and two with negative real parts for both choices of λ.

For a semi-infinite wire, defined in the region $0 < x < \infty$, we impose boundary conditions that $u = 0$ at $x = 0$ and that $u \to 0$ for $x \to \infty$. For the case $\lambda = -1$, the second requirement is satisfied if and only if we choose $a_4 = 0$. This leaves us three real parameters, a_3 and the real and imaginary parts of a_1. As the boundary condition at $x = 0$ imposes only two additional conditions on u, we can always find a nonzero choice of the coefficients a_n to satisfy all requirements. This defines the wave function for a zero-energy Majorana mode localised near $x = 0$.

For the case $\lambda = 1$, the requirements that the wave function decay for $x \to \infty$ means that three coefficients must be chosen equal to zero, corresponding to n =1, 2, and 3, leaving only one coefficient to adjust. Clearly this will not allow us to satisfy the boundary condition at $x = 0$. In the non-topological regime, there are two adjustable coefficients for either choice of λ, which means that one cannot find a nonzero solution of the equations in either case.

Returning to the topological case, and following [74], we may write

$$z_1 = -ik_F + \kappa, \tag{3.8}$$

where k_F and κ are positive and k_F reduces to the Fermi wave vector of the normal wire in the limit where the pairing potential Δ is small. The envelope of the Majorana wave function will decay exponentially for $x \to \infty$ with a decay length ξ, given by

$$\xi^{-1} = \min(\kappa, w) \tag{3.9}$$

In the limit where $E_{\rm Z}$ tends to the critical value $E_c = \sqrt{\Delta^2 + \mu^2}$ for the transition to the non-topological phase, so the energy gap vanishes at $k = 0$, one finds that $w \to 0$, and hence $\xi = w^{-1}$. However, for magnetic fields such that $E_{\rm Z}$ is larger than a second value E_2, one finds $w > \kappa$, so that $\xi = \kappa^{-1}$. In this regime, the large distance behavior of the Majorana wave function may be written

$$u(x) \sim e^{-\kappa x} \sin(k_F x + \phi), \tag{3.10}$$

where the phase shift ϕ will itself be small for large values of $E_{\rm Z}$. As was noted in [74], the crossover field B_2 is fairly close to the critical value B_c for nanowires such as InSb.

In the case of a long but finite wire, we must replace the boundary condition at infinity by the condition that the two components of u should vanish at $x = L$. For a finite wire, we no longer require $a_4 = 0$. Since a_4 must be real, however, this gives us only one additional parameter to choose, and one cannot find a non-trivial zero-energy solution for general values of the control parameters μ, B and L. On the other hand, zero-energy solutions could exist on discrete surfaces of co-dimension unity in the control parameter space.

In the regime of parameters where Eq. 3.10 applies, for the semi-infinite system, we expect to find these zero energy solutions on surfaces close to the points where $Lk_F(\mu, B) = n\pi$, where n is an integer.

If L/ξ is large compared to unity, then the magnitude of a_4 necessary to satisfy the boundary conditions at $x = L$ will be of order $e^{-L(w+\kappa)}$. The non-zero value of a_4 requires a correction to a_1, a_2 and a_3 in order to continue to satisfy the boundary conditions at $x = 0$, but this correction is obviously small when L is large.

If a non-zero wavefunction $\psi^L(x)$ is obtained in this manner for $\lambda = -1$, it can be used to construct a zero energy Majorana operator, γ^L, which will have maximum weight at the left end of the wire, and decrease exponentially for large L. We define

$$\gamma^L = \sum_\sigma \int \left[u^L_\sigma(x)\Psi_\sigma(x) + v^L_\sigma(x)\Psi^\dagger_\sigma(x)\right] \mathrm{d}x \tag{3.11}$$

In order to satisfy the requirement $(\gamma^L)^2 = 1$, the wave function must be normalized so that

$$2\sum_\sigma \int_0^L |u^L_\sigma(x)|^2 dx = 1 \tag{3.12}$$

In order to have a precise definition one must still introduce a convention with regard to the overall sign of the wave function. Here, we adopt the convention that the sign of $-iu(x)$ should be positive for x slightly greater than zero, for the spin component aligned with the applied magnetic field. For large magnetic field values, such that $\kappa < w$, this implies that

$$-iu^L_\downarrow(x) \approx C\kappa^{1/2} e^{-\kappa x} \sin(k_F x), \tag{3.13}$$

where C is a constant of order unity.

Following a similar procedure for the case $\lambda = 1$, we can construct a Majorana operator γ^R associated with the right end of the wire. Again there is an arbitrariness of an overall sign, however, we can fix the sign by choosing the wave function as

$$u^R(L-x) = -iu^L(x)\,, \quad v^R(L-x) = iv^L(x). \tag{3.14}$$

It is easy to show that u^R satisfies the necessary equations and boundary conditions for $\lambda = 1$, and that the corresponding wave function ψ^R is orthogonal to ψ^L under the BdG metric. This means that $\{\gamma^R, \gamma^L\} = 0$.

We may now form a BdG Fermion annihilation operator $\Gamma = (\gamma^R + i\gamma^L)/2$, with the corresponding BdG wave function $\psi = (\psi^R + i\psi^L)/2$. Although the charge density is zero for all x in the Majorana states ψ^R or ψ^L, the charge density associated with the wave function ψ is given by

$$\begin{aligned} \langle \rho(x) \rangle_\psi &= \frac{|v^R(x) + iv^L(x)|^2 - |u^R(x) + iu^L(x)|^2}{4} \\ &= -u^R(x)\, u^R(L-x), \end{aligned} \tag{3.15}$$

which is generally not zero. Specifically, $\langle \rho(x) \rangle_\psi$ is the difference in charge density when the state ψ changes from unoccupied to occupied.

Let L and B be fixed at specified values, and let μ_0 be a value of the chemical potential μ for which there exist zero energy states for the given L and B. Let us now consider a chemical potential $\mu = \mu_0 + \delta\mu$, where $|\delta\mu|$ is small. The system Hamiltonian will therefore be modified by the addition of a term $-\delta\mu \int \rho(x)dx$. Then the wavefunction ψ constructed above is no longer an exact solution of the BdG equations. To lowest order in $\delta\mu$, however, it remains a solution of the BdG equations, and the energy of the state is given by first order perturbation theory as $E_\psi =$

$-\delta\mu\,\delta N_\psi$, where

$$\delta N_\psi = -\int_0^L u^R(x)\,u^R(L-x)\,dx, \tag{3.16}$$

which we may interpret as the net number of electrons associated with the zero-energy level ψ.

For $\delta\mu \neq 0$, the ground state of the system will have ψ occupied if and only if $E_\psi < 0$. The relation $E_\psi = -\delta\mu\,\delta N_\psi$ implies that if $\delta\mu$ changes from a value slightly smaller than zero to a value slightly larger than zero, the total electron charge will always jump by a positive amount, given by the absolute value $|\delta N|$. It also follows that the value of the jump is given by the slope of the energy curve for $\delta\mu \to 0^+$:

$$\delta N \equiv |\delta N_\psi| = \lim_{\mu\to\mu_0^+} \frac{\partial E_\psi}{\partial \mu} \tag{3.17}$$

In the case of large B and $\kappa L > 1$, one finds for the zero energy state at $\mu = \mu_0$:

$$\langle\rho(x)\rangle_\psi \sim \kappa e^{-\kappa L}\sin^2(k_F x)(-1)^{n+1} \tag{3.18}$$

where $n = k_F L/\pi$. The net charge associated with the state is given by $\delta N_\psi \approx (-1)^{n+1}\kappa L e^{-\kappa L}$.

3.6 Numerical Calculations of Total Charge

We now calculate δN numerically, using Eq. 3.3, and examine its dependence on the applied magnetic field. The features described in Sec. 3.4 can be traced to the cosine term in the splitting between the Majorana states. The magnitude of the change in charge allows us to probe the $e^{-\kappa L}$ factor of Eq. 3.18, which also enters

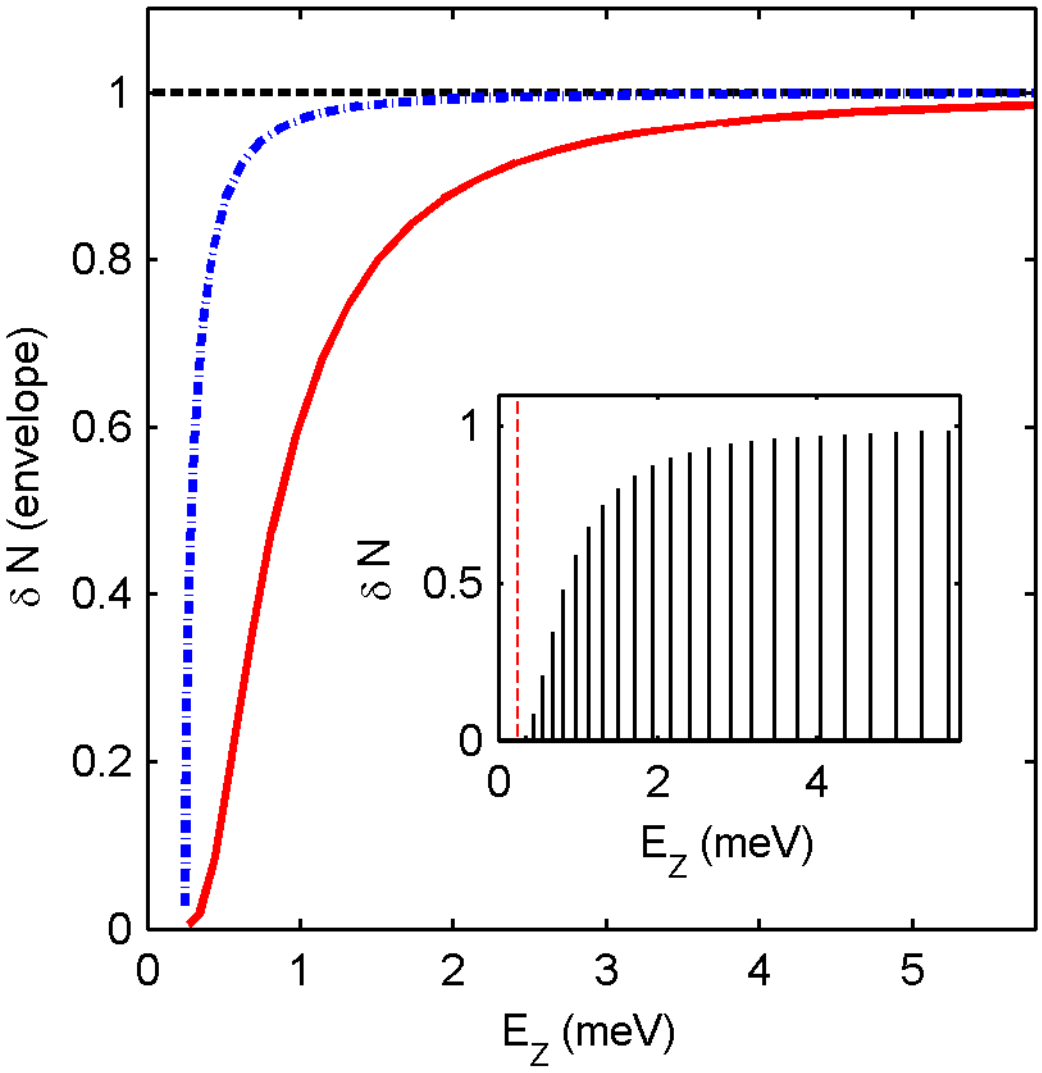

Figure 3.3: Jumps in electron number in the wire, δN, as a function of E_{Z} for $\mu = 0$. Inset: peaks corresponding to the zeros of the spectrum in the topological regime. Red dashed line is at $E_{\mathrm{Z}} = \Delta$. Main figure: trace of the maximum of the peaks with interpolation. Solid red - $\alpha > 0$, $\Delta > 0$; blue dash-dot - $\alpha = 0$, $\Delta > 0$; black dashed - $\alpha = 0$, $\Delta = 0$.

the energy splitting. From this information, we can distinguish between topological charging events and non-topological states.

In particular, consider a plot of δN in the wire at $\mu = 0$ as a function of E_{Z}, as shown in the inset in Fig. 3.3. The height of the peaks shows the magnitude of change in total charge in the wire. The positions of these peaks correspond to the parity flips at $\mu = 0$ as seen in Fig. 3.2b. At large B, the split-Majorana states saturate to one, since at high B the splitting becomes comparable to Δ, and the peaks represent discrete single-particle states. The main part of Fig. 3.3 traces and interpolates between the maxima of these peaks for the various parameter regimes discussed, all at $\mu = 0$. For a wire without an induced superconducting gap – regardless of the presence of spin-orbit interaction – the peak height is constant and peaks are visible all the way down to $B = 0$ (black dashed line in Fig. 3.3). This is as expected for a system without a gap, in which every charging event corresponds to the addition of an electron. For a system with finite induced Δ and $\alpha = 0$, we find that there are no peaks visible for $E_{\mathrm{Z}} < \Delta$, as expected when the system is gapped and there are no mid-gap states. At large $E_{\mathrm{Z}} >> \Delta$, the discrete charging events correspond to the addition of electrons, and $\delta N = 1$. As seen from the height of δN, when $E_{\mathrm{Z}} \sim \Delta$, the peaks correspond to a change in charge of less than one electron.

Although the peaks in our calculations have zero width, we note that in a real experiment, finite temperature and long parity-breaking time will both lead to larger widths for the peaks. Additionally, if we allow tunneling to a normal metal, peak width could change.

When $\alpha > 0$, the topological case, peaks begin to appear at $E_{\mathrm{Z}} \sim E_2 > \Delta$,

and the magnitude has the form of the prefactor in Eq. 3.18. Since $\kappa \sim 1/E_Z$ for $E_Z > E_2$ (see [38,74]), the dependence on the Zeeman field, solid red line in Fig. 3.3, is roughly $\exp(-L/E_Z)/E_Z$. The shape of the curve is closely linked to the overlap – and splitting – of the Majorana modes. The difference between the different traces of the amplitude height is a useful tool to distinguish between the oscillations in an experiment.

The calculations shown here are done at T=0. At finite temperatures, we expect the discrete jumps to be smeared. Since, at $\mu = 0$, $E_2 \sim E_c = \Delta$, an experiment can extract a value for Δ from a plot such as Fig. 3.3.

3.7 Numerical Calculations of the Charge Distribution

Having established that the charge in the wire changes whenever the split Majorana states are degenerate, we now examine how the charge is distributed along the wire. Since the discrete charging events within the topological regime correspond to the mid-gap state (as in Eq. 3.18), we examine the wave-function and charge of that state alone. In the BdG basis chosen above, we calculate the amplitude $|\psi(x)|^2 = |u|^2 + |v|^2$ and the charge $\langle\rho(x)\rangle_\psi = |u|^2 - |v|^2$ as a function of position along the wire. As in previous works ([38,91]), we see that the Majorana state is concentrated on the edges, as shown in the upper panel of Fig. 3.4. However, the charge corresponding to this state – when the wires overlap – is spread out along the wire (bottom of Fig. 3.4). Similar results may be seen in Fig. 6 of reference [88]. Fig. 3.4

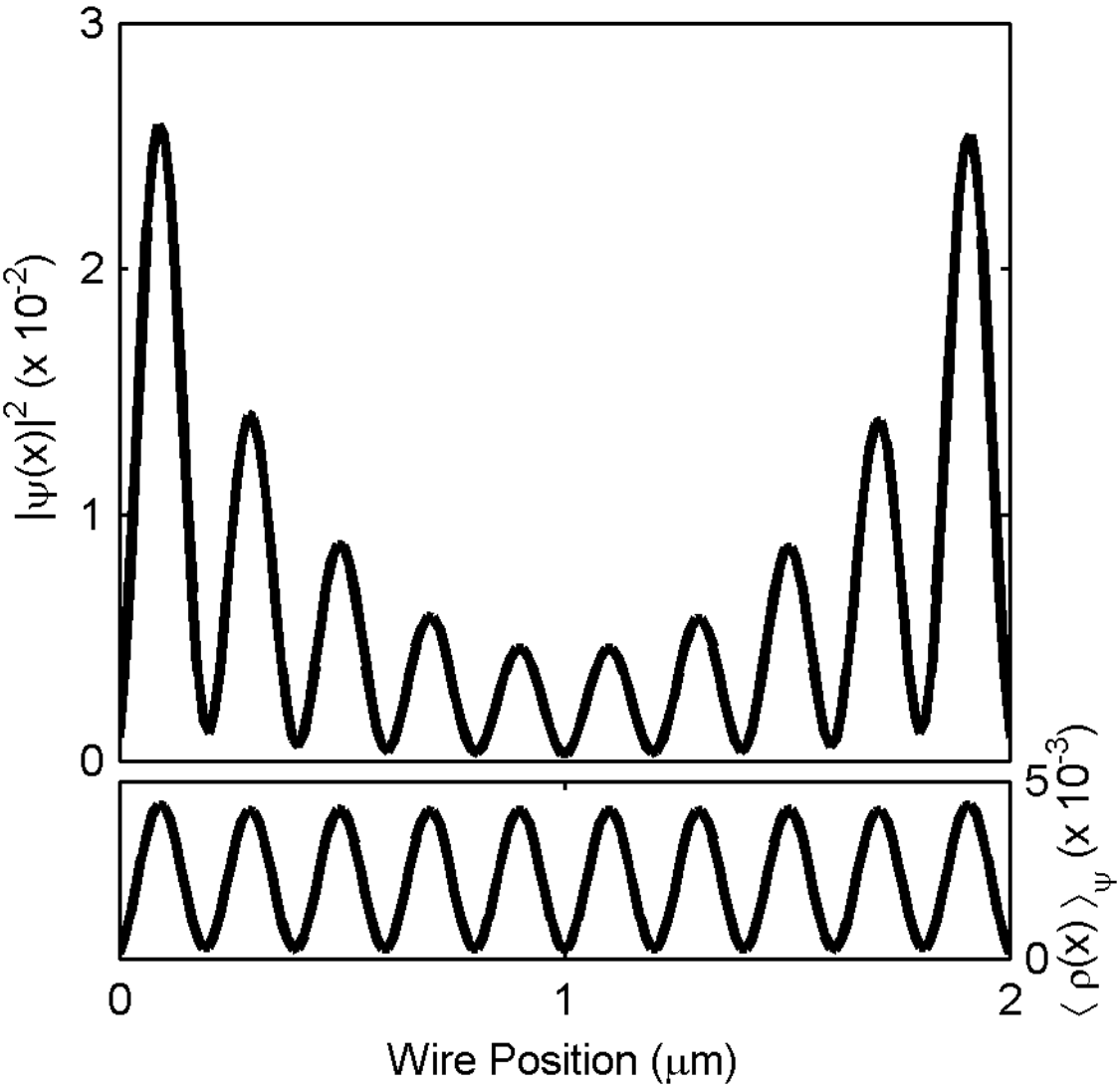

Figure 3.4: Top: Intensity $|\psi(x)|^2 = |u|^2 + |v|^2$ of the wavefunction for a Majorana-pair state whose energy crosses zero at a degeneracy point in the spectrum ($E_{\rm Z} \sim 0.69$meV). As expected, the wavefunction is concentrated at edges, and decays toward the centre. Bottom: The change in charge density, $\langle \rho(x) \rangle_\psi = |v|^2 - |u|^2$, when this state becomes occupied. The charge is small but not zero, and is spread uniformly along the wire length.

is calculated at a degeneracy point in the spectrum at $\mu = 0$ and $E_Z \sim 0.69$meV, well inside the topological regime, with $E_Z > E_2$. Near this point, the splitting decays and oscillates, as discussed in [74]. The charge is distributed sinusoidally across the wire, implying that a measurement of the charge does not need to be done near the end of the wire. Furthermore, the fact that the charge is distributed along the whole wire can be used to distinguish between the various explanations of the zero-bias conductance peak seen in transport measurement, since any non-topological causes should not have a uniform charge distribution.

3.8 Jumps in Spin Density

Jumps in parity will generally be accompanied by jumps in the electron spin density as well as the charge density. The jump in total spin $\delta < \vec{S} >$ will be given by

$$\left\langle \delta \vec{S} \right\rangle = \pm \hat{b} \frac{\partial E_\psi}{\partial E_Z}, \tag{3.19}$$

where $\hat{b}$ is a unit vector in the direction of $\vec{B}$ and the sign in front is given by the sign of δN_ψ. The ratio between $|\left\langle \delta \vec{S} \right\rangle|$ and δN is fixed by the Clausius-Clapyron relation which states $\delta \left\langle \vec{S} \right\rangle / \delta N$ is equal to the slope of $d\mu/dE_Z$ of the locus of parity jumps in the μ-E_Z plane. The discontinuity in spin density should be uniformly spread along the length of the wire in a manner similar to the jumps in charge density.

3.9 Effects of Electron-Electron Interactions

Although our calculations, so far, have been based on a model with non-interacting electrons, we present here a brief discussion of the modifications one might expect due to Coulomb interactions in a real system.

In general, one would expect that electron-electron interactions will renormalise parameters of the model, so that, e.g., μ and Δ may depend in a non-trivial way on the applied magnetic field and on the voltage applied to a nearby gate. However, we expect that a renormalised single-particle description will remain valid at low energies. Therefore, we expect that interactions will change the positions in the magnetic field and gate voltage where jumps in the number parity occur, but will not have a major effect on the size of the associated jumps in the charge of the nanowire, provided that the size is computed with a decay length ξ appropriate to the renormalised values of Δ and the Fermi velocity. Our argument that the charge jump due to change in occupancy of a zero-energy Majorana pair should be roughly uniform along the length of the wire should be unchanged. At the same time, a parity jump due to a change in occupancy of, say, a localised impurity state, would produce a charge-density change in the nanowire that would remain at least partially localised in the vicinity of the impurity. We note that due to screening by the adjacent superconductor, the effective interaction between electrons on the nanowire will be relatively short-ranged.

Of course, screening by the superconductor will reduce the charge sensitivity of a nearby SET. However, we argue, using a simple model, that this effect should not be drastic. Therefore, we expect that SET measurements could be used to study the size of charge jumps in a real experiment, and could be used to distinguish a jump

that is uniform along the wire from one that is concentrated at an impurity or at the ends of the nanowire.

Let us consider the voltage $V(y,z)$ measured at a point (x,y,z), which is a distance $R = \sqrt{y^2+z^2}$ from the axis of the nanowire, at a position x along the length of the wire, with $r_w << R << L$, where r_w is the radius of the nanowire. The electrostatic potential V at the specified point should have the form

$$V(x,y,z) = \int_0^L dx' \rho(x') K(x',x,y,z), \tag{3.20}$$

where ρ is the charge density in the nanowire and the kernel K depends on the detailed geometry. We expect that V should be most sensitive to the charge density at points where $|x'-x| \leq R$, so as a crude approximation we may write

$$V(x,y,z) \approx \tilde{\rho}(x) C(y,z) \tag{3.21}$$

where $\tilde{\rho}(x)$ is an average of the charge density over the region $|x'-x| \leq R$ and $C(y,z)$ again depends on the geometry of the system.

We may now envision an experiment with, say, three SETs, localised at different positions x but the same distance R from the wire. We may position one SET at the centre of the wire ($x = L/2$) and the other two near the ends, $x = x_0$, and $x = L - x_0$, where x_0 is larger than R but smaller than the superconducting decay length ξ. The prediction of our analysis, combined with the approximation (3.21), is that a charging event due to a change in the occupation of a zero energy Majorana pair should cause a voltage jump with the same strength at all three detectors. By contrast, if the charging event were concentrated at the two wire ends in the same way as the Majorana wave function itself, one would expect the voltage signal to be larger

at the two ends than at the central SET. If the charging event were associated with an impurity at an arbitrary point in the wire, the voltage signals would in general be different on all three SETs, and might vary randomly from one event to another.

More properly, one should not use the approximation (3.21) but rather the non-local relation (3.20) to analyse the charge distribution in the nanowire. However, if the kernel K is known, either from a calculation or from experimental calibrations, it should be relatively easy to distinguish between the different charge distributions considered above.

In order to estimate the coefficient $C(y, z)$, we consider a simplified model. We suppose that the superconductor is represented by a perfect conductor of radius r_s, parallel to the nanowire, with an axis displaced from that of the nanowire by a distance D which is of the order of $r_w + r_s$. We assume that the point x is far from the ends of the wire compared to R, so we may treat the wires as infinite. Further, we approximate the nanowire as a uniform line charge with a fixed density $\tilde{\rho}$, located on the line $y = z = 0$.

Under these assumptions, we expect an image line charge a distance d above the infinite semiconducting wire, and we expect it to lie within the cylindrical SC. For two wires (charge and image charge), we have the potential at a point (x, y, z):

$$V(y, z) = \frac{\tilde{\rho}}{4\pi\epsilon_0} \left[\ln(y^2 + z^2) - \ln(y^2 + (z - d)^2)\right] + \eta\tilde{\rho}, \tag{3.22}$$

where η is the value of the potential at infinity. We want the potential to vanish on the surface of the SC. Setting the potential to zero, we find that the potential vanishes

on a circle, and by setting the radius to be r_s, we can solve for

$$d = \frac{2r_w r_s + r_w^2}{r_s + r_w}, \tag{3.23}$$

and

$$\eta = -\frac{1}{2\pi\epsilon_0} \ln\left[1 + \frac{r_w}{r_s}\right]. \tag{3.24}$$

This gives

$$C(y,z) = \frac{1}{4\pi\epsilon_0}\left[\ln(y^2+z^2) - \ln(y^2+(z-d)^2)\right] - \frac{1}{2\pi\epsilon_0}\ln\left[1+\frac{r_w}{r_s}\right]. \tag{3.25}$$

The analysis above may be extended to the case where the charge density on the nanowire has the form

$$\rho(x) = \rho_q \cos qx, \tag{3.26}$$

where the wave vector q is assumed small compared to $1/r_w$. In this case, the charge on the superconductor will not precisely cancel the charge on the nanowire, and there will be a component of the potential which depends logarithmically on R, in the region $r_w < R < 1/q$, while the potential falls to zero for $R \gg 1/q$. More precisely, for $q \neq 0$, one finds $V(x,y,z) = K_q \rho(x)$, with

$$K_q \approx \eta\left[1 - \frac{\ln(R/r_w)}{\ln(qr_w)}\right] \tag{3.27}$$

in the region $r_w < R < 1/q$, where η is the quantity given by Eq. (3.24). Thus, K_q reduces to our previous result for $C(y,z)$, in the limit $q \to 0$, with R/r_w fixed but large. For an infinite wire, the dependence of the kernel $K(x',x,y,z)$ on the separation $x'-x$ may be obtained by taking the Fourier transform of K_q. The logarithmic dependence of K_q means that K will not fall off very rapidly for $|x'-x| \gg R$.

For $R >> d$, taking $r_s = 2r_w$ and $\tilde{\rho} = 0.1e/L$ where e is the electron charge and $L = 2\mu$m, we find $V(R) \sim 60\mu V$, which should be detectable with a SET.

So far, we have assumed implicitly that there is just a single contributing mode in the nanowire. In the case of a multi-mode wire, any charge inhomogeneity due to a localised impurity state will be further screened by the additional modes in the wire, which will tend to spread the resulting charge more uniformly along the wire. This will reduce the differences in the voltages measured by SETs at different positions along the wire, but it should not affect the average voltage signal. The extra modes should not affect the signal induced by a spatially uniform charge jump, such as predicted due to the change in occupancy of a zero-energy Majorana pair.

3.10 Experiment

As we have argued above, charge jumps in the semiconductor nanowire should be observable using a single electron transistor (SET) as a sensitive charge detector [59, 60, 88], assuming that the wire length L is not too much longer than the coherence length ξ. Furthermore, measurements at several positions – either through multiple or scanning SETs – can be done to confirm the uniform charge distribution.

We note that this measurement technique can be applied to other systems expected to have Majorana end states. In particular, Majorana states in wires made from other materials, or created within 2D topological insulators (e.g. HgTe quantum wells [92]), if realised, can hopefully be observed with an SET. Furthermore, in these systems, multiple-band concerns might be alleviated.

The results presented assume a clean system. A real system will include some

amount of disorder. We have checked that small amounts of disorder shift the parity transitions slightly, but do not change the qualitative results. Adding a large amount of disorder wipes out all the effects discussed. The effects of disorder on Majorna end states in one-dimensional wires are discussed in [93, 94].

An important experimental parameter which we hold fixed in our discussion is the wire length. For the case of a long wire, the Majorana end states are present, but the splitting between the two states is exponentially suppressed, and therefore the number-parity oscillations are harder to observe. Simultaneously however, a longer wire means smaller level spacing, and therefore more oscillations with respect to B before the splitting reaches the size of the gap. We thus conclude that there is an intermediate range ideal for experiments, where the exact length desired depends on the other system parameters. For a non-topological wire – $\alpha = 0$ or $\Delta = 0$ – the level spacing decreases with wire length, until the system is compressible everywhere in the μ-B plane. Our calculations are consistent with these expectations.

To estimate the ideal wire length, we begin by relating the energy gap and coherence length to known system parameters. For $E_{\rm Z} >> \Delta$, the gap at $k_{\rm F}$ is $E_{\rm gap} = 4\Delta\sqrt{E_{\rm SO}/E_{\rm Z}}$, where $E_{\rm SO} = \alpha^2 m$ is the spin-orbit energy scale. Using the Fermi velocity (for $\mu \sim 0$) $v_{\rm F} = p_{\rm F}/m = 2/l_{\rm SO}m = 4E_{\rm SO}l_{\rm SO}$, with $l_{\rm SO}$ the spin-orbit length, we find the coherence length $\xi = v_{\rm F}/E_{\rm gap} = l_{\rm SO}\sqrt{E_{\rm SO}E_{\rm Z}}/\Delta$. To observe the splitting, we need a wire length such that the splitting between the midgap states, $\epsilon_0 \sim E_{\rm gap}e^{-L/\xi}$, is larger than a typical temperature, say $T \sim 100mK \simeq 10\mu eV$, and also $\epsilon_0 << E_{\rm SO}$. For typical values of $E_{\rm Z} = 750\mu eV$, $E_{\rm SO} = 50\mu eV$ and $l_{\rm SO} = 200nm$, we find $E_{\rm gap} \sim 250\mu eV$. If we choose $\epsilon_0 \sim \frac{1}{5}E_{\rm gap} >> T$, we find $L \sim 250nm$.

A related possible experiment is to measure the jumps in the spin of these wires. The split Majorana states carry spin in addition to their electric charge. This spin is considerably smaller than the spin of a single electron, and therefore very difficult to detect using available experimental techniques [95, 96]. However, recent advances suggest that such measurements might not be so far off [97, 98]. With an extremely sensitive magnetometer, we can hope to pick out the oscillations in the magnetisation of the system as a function of μ and B, as discussed for the charge.

3.11 Methods for Calculating Number Parity

We discuss two equivalent numerical methods for calculating the number parity when $\Delta > 0$. The plots in Fig. 3.2 were actually obtained using the second method, but both methods were checked against each other.

The first option is to follow the energy eigenvalues along a curve in the μ-B plane, starting at a point with $B = 0$, and ending at the desired point (μ, B). We know that the number parity must be even when $B = 0$, and the number parity will flip when and only when an energy level crosses zero. Therefore, the number parity at (μ, B) is equal to $(-1)^n$, where n is the number of zero-energy crossings along the curve. Numerically, some care must be taken to correct for errors where two consecutive zeros are so close to each other that they appear as one, resulting in the wrong parity being recorded beyond the second of the close points.

As an alternative, we have used a new method, which to our knowledge has not been previously discussed in the literature. For a spinful system on a lattice with N sites, write $H = \vec{\psi}^\dagger \mathcal{H}_{\mathrm{BdG}} \vec{\psi}$, with $\vec{\psi} = (a_1, ..., a_{2N}, a_1^\dagger, ..., a_{2N}^\dagger)^T$. Then $\mathcal{H}_{\mathrm{BdG}} = U \mathcal{D} U^\dagger$,

where $U = \begin{pmatrix} u & v \\ v^* & u^* \end{pmatrix}$ is a unitary matrix and $\mathcal{D}$ is a diagonal matrix ordered so that the the first $2N$ elements are the positive energy eigenvalues. We thus have:

$$\begin{aligned} H &= \vec{\psi}^\dagger U \mathcal{D} U^\dagger \vec{\psi} \\ &= \vec{\eta}^\dagger \mathcal{D} \vec{\eta}, \end{aligned} \tag{3.28}$$

with $\vec{\eta} = (\eta_1, ..., \eta_{2N}, \eta_1^\dagger, ..., \eta_{2N}^\dagger)^T$. We claim that the parity of the system is $P = (-1)^q$, where $q = \text{rank}(v)$ mod2. We have checked this numerically for $\Delta \geq 0$, and prove it for $\Delta = 0$, along with a slightly different version of the claim for the case $\Delta > 0$. In particular, for $\Delta > 0$, we will show that $\det(v) \neq 0$ if and only if the system is in an even-parity state, subject to the following assumption, which we find compelling. Specifically, since the pairing term in the Hamiltonian does not conserve electron number, we assert that a ground state with even number parity should contain some admixture of states with every possible even electron number between zero and $2N$, including the single basis state with $2N$ electrons present. Thus, we shall assume that if the ground state $|G\rangle$ has even number parity, then

$$\langle G | \, a_1^\dagger \cdots a_{2N}^\dagger \, |0\rangle \neq 0. \tag{3.29}$$

Begin Proof $\Delta = 0$

In the absence of a pairing potential an occupied eigenstate of $\mathcal{H}_{\text{BdG}}$ corresponds to a vanishing column in u and a non-zero column in v, whereas for an unoccupied eigenstate the converse is true. This means that the number of occupied states n_{occ} simply equals the number of non-zero columns in v which, since U is unitary, are all linearly independent. One then has by definition that $n_{\text{occ}} = \text{rank}(v)$, and in particular $q = \text{rank}(v)$ mod2 as claimed.

Begin Proof $\Delta > 0$

Consider the state

$$|G'\rangle \equiv \eta_{2N} \cdots \eta_1 |0\rangle . \tag{3.30}$$

Since any η_i operating on this state annihilates it, $|G'\rangle$ must be proportional to the ground state, unless it is identically zero. That is, $|G'\rangle = C|G\rangle$, for some constant C. Furthermore, if we transform the η_i's in (3.30) back to the electron operator basis, it is straightforward to show that the term $a_1^\dagger \cdots a_{2N}^\dagger |0\rangle$ occurs with a coefficient equal to $\det(v)$. According to our assumption (3.29), this term cannot have zero weight in the even-parity ground state, and therefore $\det(v) \neq 0$, which further implies that v must have maximal rank.

Conversely, if $\det(v) = 0$, then the system does not have a component containing $2N$ electrons, so by our assertion, it cannot be an even-parity state. We thus have that $\det(v) \neq 0$ if and only if the number parity of the ground state is even.

Although this result is sufficient for our purposes, if we make an assumption analogous to (3.29) for the case where the ground state has odd number parity, namely that the $2N-1$ electron state must have non-zero weight in the ground state, we see that the pre-factor in the expansion from $(2N-1)$ η_i's to the electron operator basis must be non-zero. In particular, one can show that the pre-factor of the leading term is now a weighted sum of the first minors of the matrix v, and by the same argument as above it cannot vanish. A vanishing determinant with a non-vanishing first minor implies that a matrix has rank one less than its maximal rank, and so for the odd case, $\text{rank}(v) = 2N-1$. Since v has size $2N \times 2N$, we see that the ground state number parity is given by $P = (-1)^q$, where $q = \text{rank}(v) \bmod 2$, as claimed.

3.12 Conclusion

In short topological wires, the predicted zero-energy Majorana end modes are split due to the significant overlap of their wavefunctions. The split states carry charge, which can be detected in experiments. Whereas the tunneling density of states measured in transport experiments is only an end effect, the charge of the split Majoranas is uniformly distributed along the wire. Comparing both charge and tunneling experiments at the end and bulk of a wire can thus resolve remaining unanswered questions in the field.

Chapter 4

Induced Superconductivity and Spin-Orbit Coupling

4.1 Motivation - HgTe

HgTe quantum wells are predicted to host localised Majorana Fermions when subjected to appropriate conditions [68, 99]. One of the necessary conditions is proximity-induced superconductivity, typically done by connecting superconducting contacts to the sample. When superconductivity is induced through contact with a superconductor, the strength of the induced potential decays away from the contacts [100]. We examine how this decay behaves in a system with strong spin-orbit coupling – another essential ingredient for the creation of localised Majorana Fermions – under the application of external in-plane magnetic fields. This work is motivated by recent experiments [101], in which the induced superconductivity in HgTe quantum wells is seen to have a novel dependence on applied magnetic fields.

4.2 Model

Since we are interested in the effects of spin-orbit coupling and magnetic fields on the induced superconductivity, rather than the effects of HgTe's band structure, we consider a two-dimensional one-band normal metal with strong Rasbha spin-orbit coupling. We place two parallel superconducting strips along this metal substrate as shown in figure 4.1, and apply in-plane fields in both the x and y directions, but no perpendicular magnetic field. The contacts are separated by a distance w, and we take

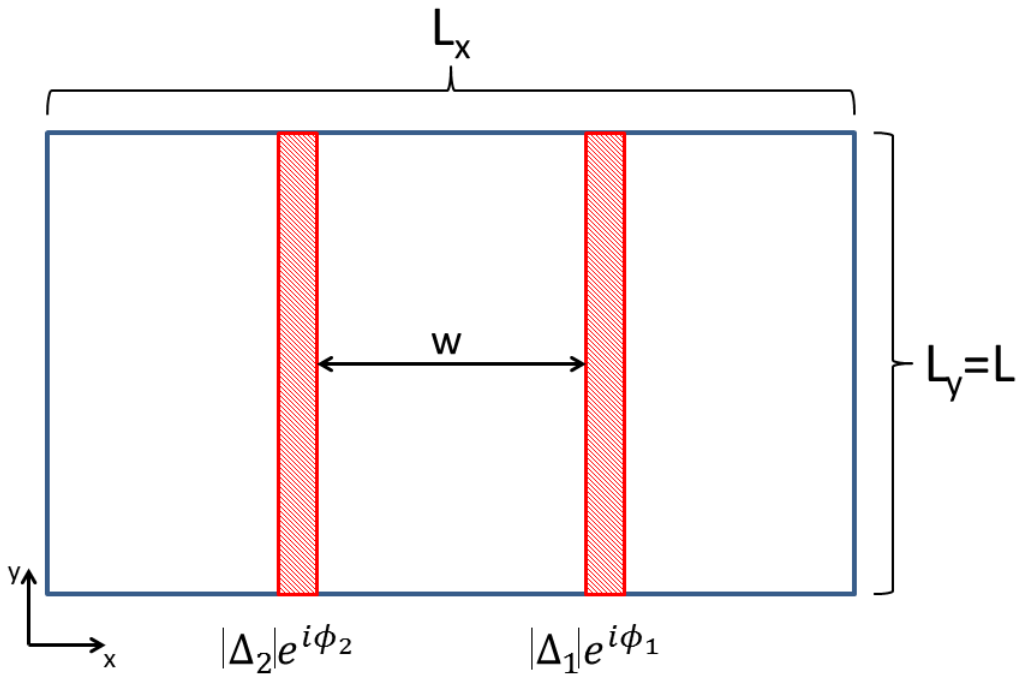

Figure 4.1: System setup. The red shaded regions are the superconducting contacts, sitting on a 2D normal-metal substrate.

periodic boundary conditions. The superconducting contacts give rise to a pairing

potential which we represent as $\Delta(\vec{x}) = \Delta_1\delta(x) + \Delta_2\delta(x-w)$, where $\Delta_i = |\Delta_i|e^{i\phi_i}$ with ϕ_1 and ϕ_2 the phases of the superconductors, and we have taken the limit of narrow wires for simplicity. Our quest is to calculate terms in the total energy per unit length, $E(\phi)$, that depend on $\phi = (\phi_1 - \phi_2)$, in the limit of an infinite system (w finite), since these terms give the strength of the induced pairing potential in the sample. From these terms, we can calculate the Josephson current, $(2e)\frac{\partial E}{\partial \phi}$. The maximum of the Josephson current is the critical current, which can be measured, and has already been measured in HgTe quantum wells [47].

We begin by calculating the eigenstates of the system from the Bogoliubov de Gennes equations, and if we assume that the coupling to the superconductors is weak, we can simplify the problem and use perturbation theory. If Δ_2 is small, then by using first order perturbation theory, we see that to lowest order, $E(\phi)$ is given by

$$E(\phi) = \Delta_2^* \left\langle \psi_\uparrow(w)\psi_\downarrow(w) \right\rangle_{\Delta_1} + \text{C.C.}, \tag{4.1}$$

where $\left\langle \psi_\uparrow(w)\psi_\downarrow(w) \right\rangle_{\Delta_1}$ is calculated in the presence of Δ_1, with $\Delta_2 = 0$. When Δ_1 is small, $\left\langle \psi_\uparrow(w)\psi_\downarrow(w) \right\rangle_{\Delta_1} \sim \Delta_1$, which gives $E(\phi) \sim \Delta_2^*\Delta_1 + \text{C.C.} \sim \cos\phi$ as the phase dependence. We also work out the dependence on the other system parameters.

We assume that the system is translationally invariant and infinite in the y direction, and can reduce our sums to integrals.

4.3 Scattering

To calculate the expectation values described in the previous section, we treat the contacts as delta-functions in x and extending in y, and calculate the scattering

amplitudes for the plane waves off of this potential. By assuming that the scattering is weak, we can still consider the periodic boundary conditions to be satisfied by the incoming wave alone. Furthermore, since the coupling is assumed to be weak, we only keep terms to lowest order in Δ_1, having set Δ_2 initially to zero.

The Hamiltonian without the potential is

$$H_0 = \begin{pmatrix} H_{\mathrm{e}} & 0 \\ 0 & H_{\mathrm{h}} \end{pmatrix}, \tag{4.2}$$

with H_{e}, the electron part,

$$H_{\mathrm{e}} = \begin{pmatrix} \frac{-\nabla^2}{2m} - \mu - \epsilon & B_x - iB_y + (-i(-i\partial_x) - (-i\partial_y))\, R_0 \\ B_x + iB_y + (i(-i\partial_x) - (-i\partial_y))\, R_0 & \frac{-\nabla^2}{2m} - \mu - \epsilon \end{pmatrix}, \tag{4.3}$$

and the hole part

$$H_{\mathrm{h}} = \begin{pmatrix} -\frac{(-\nabla^2)}{2m} + \mu - \epsilon & -B_x - iB_y + (i(-i\partial_x) - (-i\partial_y))\, R_0 \\ -B_x + iB_y + (-i(-i\partial_x) - (-i\partial_y))\, R_0 & -\frac{(-\nabla^2)}{2m} + \mu - \epsilon \end{pmatrix}. \tag{4.4}$$

In both terms, m is the effective mass, μ is the chemical potential, ϵ is the BdG energy measured relative to the Fermi level, B_x and B_y are magnetic fields, and R_0 is the strength of the Rashba spin-orbit coupling. We have doubled our basis (as usual for a BdG Hamiltonian), writing $\vec{\Phi} = (u_\uparrow, u_\downarrow, v_\uparrow, v_\downarrow)^T$, and we have $H_0\vec{\Phi} = 0$, since we have already included ϵ in the definition of H_0.

As a starting point, we can solve this Hamiltonian without the superconductor. Using the fact that the system is translationally invariant in this case, we can impose periodic boundary conditions and solve the system in k-space and obtain plane wave

solutions. Solutions of $H_0\vec{\Phi} = 0$ require that for fixed ϵ, we choose $\vec{k}$ such that $\det(H_{BdG}) = 0$. For H_0, this means that either $\det(H_{\rm e}) = 0$ or $\det(H_{\rm h}) = 0$. Since we will eventually be interested in scattering along the x-direction while maintaining translational invariance in y, we we will consider k_x as a function of k_y, and we can later integrate over k_y.

There will be a total of eight allowed k_x values for a fixed ϵ and a given set of system parameters, four for electrons, k_x^e, and four for holes, k_x^h. For both electrons and holes, there will be two positive values of k_x, and two negative values. To keep track of the various wave-vectors and to provide some intuition for the calculation, we make the following assumptions and definitions. If we take $\epsilon = 0$ and $\Delta = 0$, and assume $\vec{B}$ and R_0 to be small, we can write the electron part of the Hamiltonian as

$$H_{\vec{k}}^0 = v_F \left[k - k_F + \vec{\beta}(\theta) \cdot \vec{\sigma} \right], \tag{4.5}$$

where $v_F = k_F/m$, $\vec{k} = [k_x, k_y] = [k\cos\theta, k\sin\theta]$, and

$$v_F\vec{\beta}(\theta) = \left[B_x + R_0 k_F \cos\theta, B_y + R_0 k_F \sin\theta \right]. \tag{4.6}$$

We define θ such that $\sin\theta = k_y/k_F$, and $-\pi/2 < \theta < \pi/2$. We want to find plane wave solutions that satisfy $H_{\vec{k}}^0\Psi = 0$. For electrons, at $\epsilon = 0$ and fixed k_y, we have four independent solutions for k_x, which we label $k_{x\eta s}^e$, where $\eta = \hat{\beta} \cdot \vec{\sigma} = \pm 1$, and

$s = \pm 1$. The solutions are:

$$\begin{aligned} k^e_{x++} &= \cos\theta \left[k_F + \frac{|\beta(\theta)|}{\cos^2\theta} \right] \\ k^e_{x-+} &= \cos\theta \left[k_F - \frac{|\beta(\theta)|}{\cos^2\theta} \right] \\ k^e_{x+-} &= -\cos\theta \left[k_F + \frac{|\beta(\pi-\theta)|}{\cos^2\theta} \right] \\ k^e_{x--} &= -\cos\theta \left[k_F - \frac{|\beta(\pi-\theta)|}{\cos^2\theta} \right] \end{aligned} \tag{4.7}$$

When spin-orbit and magnetic fields are absent ($\beta = 0$), we see that there is a degeneracy between the allowed wave-vectors. Furthermore, when either $R_0 = 0$ or $\vec{B} = 0$, $|\beta|$ is independent of θ, and the wave-vectors come in plus-minus pairs. However, when $\vec{B}$ and R_0 are both non-zero, one finds generally that there is a splitting between the $s = \pm 1$ states.

Similarly, there are four solutions for the holes, which are related to the electron solutions by $k^h_{x\eta\pm} = -k^e_{x\eta\mp}$, where with this convention, the sign of s gives the correct sign of k_x for both electrons and holes.

We define eigenfunctions for the electrons, which are spinors, $\chi^e_{\eta s}$, which satisfy the equations

$$\begin{aligned} \text{for } s = +1: &\quad \left[1 + \eta \hat{\beta}(\theta) \cdot \vec{\sigma} \right] \chi^e_{\eta+} = 0 \\ \text{for } s = -1: &\quad \left[1 - \eta \hat{\beta}(\pi-\theta) \cdot \vec{\sigma} \right] \chi^e_{\eta-} = 0, \end{aligned} \tag{4.8}$$

and are normalised such that $\sum_{\sigma=\pm1} |\chi^e_{\eta s,\sigma}|^2 = 1$. The analogous equations for the holes are

$$\begin{aligned} \text{for } s = +1: &\quad \left[1 + \eta \hat{\beta}(\theta+\pi) \cdot \vec{\sigma} \right] \chi^h_{\eta+} = 0 \\ \text{for } s = -1: &\quad \left[1 - \eta \hat{\beta}(-\theta) \cdot \vec{\sigma} \right] \chi^h_{\eta-} = 0. \end{aligned} \tag{4.9}$$

For finite $\epsilon \neq 0$, but still small, the eigenfunctions are unchanged, but the wavevectors are modified as:

$$\tilde{k}^e_{x\eta s}(\epsilon) = k^e_{x\eta s} + \frac{\epsilon s}{v_F \cos\theta} \tag{4.10}$$
$$\tilde{k}^h_{x\eta s}(\epsilon) = k^h_{x\eta s} - \frac{\epsilon s}{v_F \cos\theta}.$$

For $\Delta_1 = 0$, we can choose an orthonormal set of plane waves with $\epsilon \leq 0$, so

$$u_\sigma(x) = \frac{1}{\sqrt{L_x L_y}} \chi^e_{\eta s,\sigma} e^{i\left[k^e_{x\eta s} + \frac{\epsilon s}{v_F \cos\theta}\right]x} \tag{4.11}$$

$$v_\sigma(x) = 0. \tag{4.12}$$

When $\Delta_1 \neq 0$, u_σ is unchanged to first order in Δ_1, but we obtain a hole component:

$$v_\sigma(x) = \sum_{\eta'} A_{\eta\eta'} e^{i\left[k^h_{x\eta' s} - \frac{\epsilon s}{v_F \cos\theta}\right]x} \chi^h_{\eta' s,\sigma}, \text{ for } xs > 0, \tag{4.13}$$
$$v_\sigma(x) = \sum_{\eta'} B_{\eta\eta'} e^{i\left[k^h_{x\eta' s} - \frac{\epsilon s}{v_F \cos\theta}\right]x} \chi^h_{\eta' s,\sigma}, \text{ for } xs < 0,$$

where $A_{\eta\eta'}$ and $B_{\eta\eta'}$ are determined by the boundary conditions at $x = 0$, and depend on k_y but not on ϵ. When B_x, B_y and R_0 are small, these coefficients depend on their relative magnitudes, but not on their absolute values, and are proportional to $\Delta_1/\sqrt{L_x L_y}$. Then for a given state, j, with fixed ϵ and k_y and incoming η, we have

$$\begin{aligned}\langle \psi_\uparrow(x)\psi_\downarrow(x)\rangle^j_{\Delta_1} &= \frac{1}{2}\left[u^*_\uparrow(x)v_\downarrow(x) - u^*_\downarrow(x)v_\uparrow(x)\right] \\ &= \frac{1}{2}\sum_{\eta'\sigma\sigma'} A_{\eta\eta'} e^{-i\Phi^{\eta\eta'}_s}\left[(\chi^e_{\eta s,\sigma})^*(\chi^h_{\eta' s,\sigma'})(i\sigma^y_{\sigma\sigma'})\right], \text{ for } xs > 0, \\ &= \frac{1}{2}\sum_{\eta'\sigma\sigma'} B_{\eta\eta'} e^{-i\Phi^{\eta\eta'}_s}\left[(\chi^e_{\eta s,\sigma})^*(\chi^h_{\eta' s,\sigma'})(i\sigma^y_{\sigma\sigma'})\right], \text{ for } xs < 0\end{aligned} \tag{4.14}$$

where

$$\begin{aligned}\Phi_s^{\eta\eta'} &= \left[\tilde{k}^h_{x\eta s}(\epsilon) - \tilde{k}^e_{x\eta s}(\epsilon)\right] x \\ &= \left[\frac{2\epsilon s}{v_F \cos\theta} + \frac{\eta|\beta(\theta)|}{\cos\theta} + \frac{\eta'|\beta(\pi-\theta)|}{\cos\theta}\right].\end{aligned} \tag{4.15}$$

We will need to integrate over ϵ and k_y. At fixed k_y, we must integrate $\int_{-\infty}^{0} d\epsilon e^{i\Phi_s^{\eta\eta'}(\epsilon)}$. If $k_F w >> 1$, the integrand is a rapidly oscillating function of ϵ when ϵ is of order E_F, so we can expand $\Phi_s^{\eta\eta'}(\epsilon)$ to first order in ϵ, and perform the integral easily, giving:

$$\int_{-\infty}^{0} d\epsilon e^{i\Phi_s^{\eta\eta'}(\epsilon)} = e^{i\Phi_s^{\eta\eta'}(0)} \left(\frac{s v_F \cos\theta}{2iw}\right). \tag{4.16}$$

For the numerical calculation that follows, we introduce the following notation.

$$\begin{aligned} k^e_{x1} &= k^e_{x++} \\ k^e_{x2} &= k^e_{x+-} \\ k^e_{x3} &= k^e_{x-+} \\ k^e_{x4} &= k^e_{x--} \end{aligned} \tag{4.17}$$

The situation is the same for the holes after the transformation defined above. Note that for electrons, $k^e_x > 0$ corresponds to a right-moving wave, whereas for holes, $k^h_x > 0$ is a left-moving wave. This is sketched in figure 4.2

With the bare problem solved, we can now add the superconducting scattering

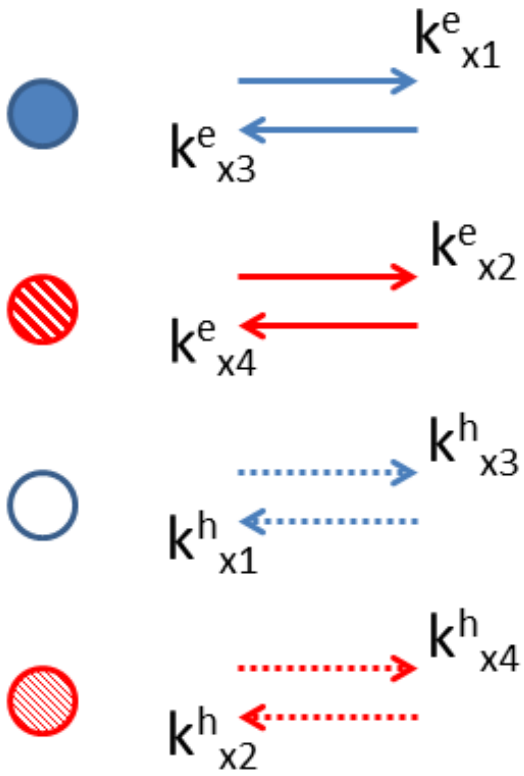

Figure 4.2: Notation choice. Solid lines for electrons. Colour/shading represent the two spin-states.

potential. The scattering potential is:

$$\begin{pmatrix} 0 & 0 & 0 & -e^{-i\phi_1}|\Delta_1| \\ 0 & 0 & e^{-i\phi_1}|\Delta_1| & 0 \\ 0 & e^{i\phi_1}|\Delta_1| & 0 & 0 \\ -e^{i\phi_1}|\Delta_1| & 0 & 0 & 0 \end{pmatrix} \delta(x). \tag{4.18}$$

From here, we can solve for the scattering amplitudes, and calculate $\langle\psi_\uparrow(w)\psi_\downarrow(w)\rangle_{\Delta_1}$. For any given energy state, we can calculate $\langle\psi_\uparrow(w)\psi_\downarrow(w)\rangle_{\Delta_1}$ in terms of u^* and v. We then sum over all occupied states j, with $\epsilon_j < 0$. For clarity, note that if $\Delta_1 = 0$ and there is no spin-orbit or magnetic field, then for $\epsilon_j < 0$, $k_e < k_F$ while $k_h > k_F$, and electron and hole states do not mix.

We have eight waves on each side of the potential, four incoming and four outgoing (two each for electrons and holes). We assume continuity of the wavefunction across the potential, and as for a standard delta-function potential, we integrate the Schrödinger equation across $\delta(x)$ to give the other boundary condition:

$$\begin{aligned} \frac{1}{2m}\left[\partial_x u_\sigma(0^+) - \partial_x u_\sigma(0^-)\right] - \sigma\Delta_1^* v_{-\sigma}(0) = 0, \\ \frac{1}{2m}\left[\partial_x v_\sigma(0^+) - \partial_x v_\sigma(0^-)\right] + \sigma\Delta_1 u_{-\sigma}(0) = 0. \end{aligned} \tag{4.19}$$

For small Δ_1, the periodic boundary conditions can still be satisfied for the incoming wave, and we can use the waves to solve for the scattered states.

For each of the four species (spin and electron/hole) of unperturbed right-moving waves from say the left-side, we assume an incoming wave with a prefactor of unity, and find an admixture of order Δ_1 in the scattered part of opposite electron/hole type on both the left and right sides of the potential. Scattering in the same electron/hole

channel is order $(\Delta_1)^2$, and we therefore neglect it. In this limit, the transmitted wave of the same spin and type as the incoming wave also has amplitude unity, as per the discussion preceding equation 4.13.

The amplitudes of the scattered waves can be calculated analytically, and after a rotation back to the original basis, we can extract the u's and v's. In general, the analytic expressions for the amplitudes can be quite involved, since they depend on all the system parameters, as well as the various k_x values.

As an example, we show the result for $B_y = 0$, if we start with an incoming electron with wave-vector k^e_{x1} with amplitude one, and fixed k_y and ϵ. We find :

$$\left\langle u^*_\downarrow(x)v_\uparrow(x)\right\rangle^j_{\Delta_1} = e^{-ik^e_{x1}x}m\Delta_1\Bigg[e^{ik^h_{x1}x}\cdot \frac{i\left(\sqrt{\left(B_x^2-2B_xk_yR_0+R_0^2k_F^2\right)\left(B_x^2+2B_xk_yR_0+R_0^2k_F^2\right)}+B_x^2+2iB_xk_xR_0-R_0^2k_F^2\right)}{(k^h_{x1}-k^h_{x3})(B_x+iR_0(k_x+ik_y))\sqrt{B_x^2+2B_xk_yR_0+R_0^2k_F^2}} + \frac{e^{ik^h_{x2}x}\left(\frac{i\sqrt{B_x^2-2B_xk_yR_0+R_0^2k_F^2}}{B_x+iR_0(k_x+ik_y)}-\frac{i\sqrt{B_x^2+2B_xk_yR_0+R_0^2k_F^2}}{B_x+R_0(k_y-ik_x)}\right)}{(k^h_{x2}-k^h_{x4})}\Bigg] \tag{4.20}$$

The expression for $\left\langle u^*_\uparrow(w)v_\downarrow(w)\right\rangle_{\Delta_1}$ will be of order Δ_1, since for either u or v order unity (incoming wave), the other must be order Δ_1. For any incoming wave-vector, there will be two relevant scattered waves that need to be considered along with the corresponding amplitudes. All of these terms must be summed for the different incoming waves to find the correct final expressions, although the prefactors depend on system parameters, and may be zero in some cases.

To sum over all states, we convert the k_x sum to an integral over ϵ as in equation 4.16, and note that besides pulling out a factor of $1/iw$, the integral leaves us

with a sum over k_y at the Fermi surface. We perform the ϵ integral by assuming $k_F w >> 1$, and expanding $k_x^{(e)} - k_x^{(h)}$ to first order in ϵ. Along the Fermi surface, we then have the k_y sum for $k_y < k_F$, which we do numerically with a cut-off just below k_F. This is justified since near $k_y = k_F$, the integrand is rapidly oscillating and therefore gives only a small contribution to the final result.

4.4 Results

When there is no magnetic field and no spin-orbit coupling, the induced superconductivity falls off as $1/w$, as expected from previous work [100]. With only a magnetic field, the Josephson coupling energy, $-E(\phi = 0)$, decreases with w, but also oscillates with increasing B, and the result is independent of the direction of the in-plane field, as shown by the blue and black solid lines in figure 4.3, which are identical. This is similar to results in superconductor-ferromagnet junctions discussed in [102, 103]. For all of figure 4.3, curves are normalised to the value for $R_0 = 0$ and $\vec{B} = 0$.

If we imagine a system in which the strength of the spin-orbit coupling can be tuned, we find no oscillations as a function of this coupling at zero external field. All calculations were done numerically for the figures.

To include B_y, we solve the k_y integral numerically, by cutting off the integral at $k_{max} \sim 0.96 k_F$. This is justified by the fact that near $k_y = k_F$, the integrand is rapidly oscillating, and therefore should not contribute significantly to the integral. The (messy) expressions for k_x can be found analytically using computer software.

The green dashed line in figure 4.3 shows the Josephson coupling as a function

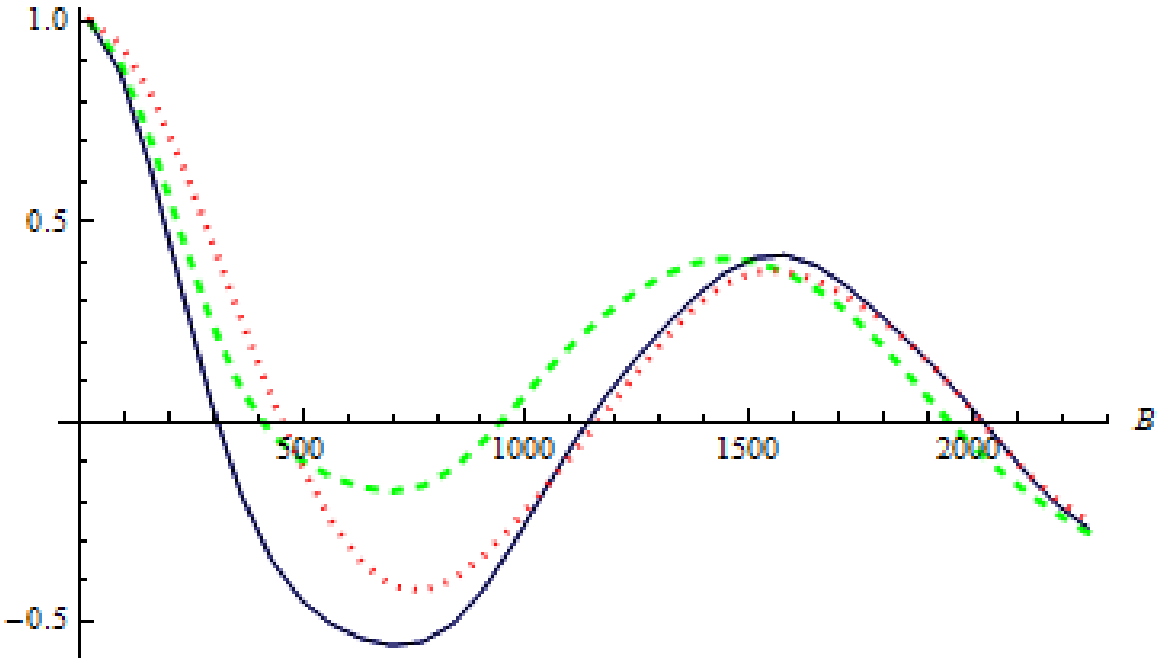

Figure 4.3: Josephson coupling energy, $-E(\phi = 0)$, as a function of B. Blue and black solid lines (identical) are without spin-orbit with respect to B_x and B_y respectively. Green dashed line is at finite R_0, only B_x. Red dotted line is at finite R_0, only B_y. Curves are normalised to the value for $R_0 = 0$ and $\vec{B} = 0$. Parameter values are given in the text

of B_x with spin-orbit coupling included (B_y=0). Note that the period and amplitude have been affected by the spin-orbit. The red dotted line in the same figure shows the pair potential versus B_y with spin-orbit coupling ($B_x = 0$). Again both the period and amplitude are changed from the $R_0 = 0$ case, and note in addition that it is distinct from when the field was in the other direction. We thus see that with spin-orbit, the induced superconductivity depends differently on the two field directions.

Figure 4.3 was plotted using the following parameter values, inspired by values in the literature [104]: $\mu = 18.7\text{meV}$, $1/2m = 1.2\text{eVnm}^2$, $w = 1200nm$, $k_F = 0.125\text{nm}^{-1}$, and $0 < B < 1\text{meV}$. Until now in this chapter, we have been using B as an energy. If we take a g-factor $g = 20$, then $B = 1\text{meV}$ corresponds to a field strength of roughly 0.86T. The value of R_0 for the dashed and dotted curves in figure 4.3, $R_0 = 0.002\text{eVnm}$, is probably smaller than is appropriate for a HgTe well, but was chosen to illustrate the situation where spin orbit and Zeeman energies have comparable magnitudes.

Bibliography

[1] Leon Balents, Physics **4**, 36 (2011).

[2] J.M. Leinaas and J. Myrheim, Il Nuovo Cimento B Series 11 **37**, 1 (1977).

[3] Frank Wilczek, Phys. Rev. Lett. **48**, 1144 (1982).

[4] F. E. Camino, Wei Zhou, and V. J. Goldman, Phys. Rev. B **72**, 075342 (2005).

[5] Chetan Nayak, Steven H. Simon, Ady Stern, Michael Freedman, and Sankar Das Sarma, Rev. Mod. Phys. **80**, 1083 (2008).

[6] Daijiro Yoshioka, in *The Quantum Hall Effect*, edited by K. von Klitzing H-J. Queisser R. Merlin H. Stormer M. Cardona, P. Fulde (Springer, Germany, 1998).

[7] J.K. Jain, *Composite Fermions* (CAMBRIDGE UNIVERSITY PRESS, UK, 2007).

[8] R. B. Laughlin, Phys. Rev. Lett. **50**, 1395 (1983).

[9] F. D. M. Haldane, Phys. Rev. Lett. **51**, 605 (1983).

[10] B I Halperin, P A Lee, and N. Read, Phys. Rev. B **47**, 7312 (1993).

[11] R. Willett, J. P. Eisenstein, H L Stormer, D C Tsui, A C Gossard, and J H English, Phys. Rev. Lett. **59**, 1776 (1987).

[12] Gregory Moore and Nicholas Read, Nuclear Physics B **360**, 362 (1991).

[13] Parsa Hassan Bonderson, Ph.D. thesis, CalTech, 2007.

[14] S S Lee, S Ryu, C. Nayak, and M P A Fisher, Phys. Rev. Lett. **99**, 236807 (2007).

[15] M. Levin, B. I. Halperin, and B. Rosenow, Phys. Rev. Lett. **99**, 236806 (2007).

[16] N. Read and Dmitry Green, Phys. Rev. B **61**, 10267 (2000).

[17] B I Halperin, Helv. Phys. Acta. **56**, 75 (1983).

[18] R. H. Morf, Phys. Rev. Lett. **80**, 1505 (1998).

[19] M Storni, R. H. Morf, and S. Das Sarma, Phys. Rev. Lett. **104**, 076803 (2010).

[20] V. J. Goldman and B. Su, Science **267**, 1010 (1995).

[21] R. de Picciotto, M. Reznikov, M. Heiblum, V. Umansky, and D. Bunin, G. Mahalu, Nature (London) **389**, 162 (1997).

[22] L. Saminadayar, D. Glattli, Y. Jin, and B. Etienne, Phys. Rev. Lett. **79**, 2526 (1997).

[23] Vivek Venkatachalam, Amir Yacoby, Loren Pfeiffer, and Ken West, Nature **469**, 185 (2011).

[24] M. Dolev, M. Heiblum, V. Umansky, A. Stern, and D. Mahalu, Nautre **452**, 829 (2008).

[25] R. L. Willett, L. N. Pfeiffer, and K. W. West, Proceedings of the National Academy of Sciences **106**, 8853 (2009).

[26] S. Ilani, A. Yacoby, D. Mahalu, and Hadas Shtrikman, Phys. Rev. Lett. **84**, 3133 (2000).

[27] J.D. Sau, R.M. Lutchyn, S. Tewari, and S. Das Sarma, Phys. Rev. Lett. **104**, 040502 (2010).

[28] Yuval Oreg, Gil Refael, and Felix von Oppen, Phys. Rev. Lett. **105**, 177002 (2010).

[29] Roman M. Lutchyn, Jay D. Sau, and S. Das Sarma, Phys. Rev. Lett. **105**, 077001 (2010).

[30] V. Mourik, K. Zuo, S. M. Frolov, S. R. Plissard, E. P. A. M. Bakkers, and L. P. Kouwenhoven, Science **336**, 1003 (2012).

[31] Anindya Das, Yuval Ronen, Yonatan Most, Yuval Oreg, Moty Heiblum, and Hadas Shtrikman, Nat Phys **8, 12**, 887 (2012).

[32] H. O. H. Churchill, V. Fatemi, K. Grove-Rasmussen, M. T. Deng, P. Caroff, H. Q. Xu, and C. M. Marcus, Phys. Rev. B **87**, 241401 (2013).

[33] W. Chang, V. E. Manucharyan, T. S. Jespersen, J. Nygård, and C. M. Marcus, Phys. Rev. Lett. **110**, 217005 (2013).

[34] MT Deng, CL Yu, GY Huang, M Larsson, P Caroff, and HQ Xu, Nano Lett. **12**, 6414 (2012).

[35] Leonid P. Rokhinson, Xinyu Liu, and Jacek K. Furdyna, Nat. Phys. **8**, 795 (2012).

[36] Eduardo J. H. Lee, Xiaocheng Jiang, Manuel Houzet, Ramon Aguado, Charles M. Lieber, and Silvano De Franceschi, Nat Nano **9**, 79 (2014).

[37] J. Alicea, Y. Oreg, G. Refael, F. Von Oppen, and M.P.A. Fisher, Nat. Phys. **7**, 412 (2011).

[38] B I Halperin, Y. Oreg, A. Stern, G. Refael, J. Alicea, and F. von Oppen, Phys. Rev. B **85**, 144501 (2012).

[39] M. Z. Hasan and C. L. Kane, Reviews of Modern Physics **82**, 3045 (2010).

[40] Xiao-Liang Qi and Shou-Cheng Zhang, Reviews of Modern Physics **83**, 1057 (2011).

[41] C. L. Kane and E. J. Mele, Phys. Rev. Lett. **95**, 146802 (2005).

[42] Markus Koenig, Hartmut Buhmann, Laurens W. Molenkamp, Taylor Hughes, Chao-Xing Liu, Xiao-Liang Qi, and Shou-Cheng Zhang, Journal of the Physical Society of Japan **77**, 031007 (2008).

[43] B. Andrei Bernevig, Taylor L. Hughes, and S.C. Zhang, Science **314**, 1757 (2006).

[44] B. Andrei Bernevig and Shou-Cheng Zhang, Physical Review Letters **96**, 106802 (2006).

[45] Markus Konig *et al.*, Science **318**, 766 (2007).

[46] Andreas Roth *et al.*, Science **325**, 294 (2009).

[47] Sean Hart, Hechen Ren, Timo Wagner, Philipp Leubner, Mathias Muhlbauer, Christoph Brune, Hartmut Buhmann, Laurens W. Molenkamp, and Amir Yacoby, Nat Phys **10**, 638 (2014).

[48] John H. Davies, *The Physics of Low-Dimensional Systems* (Cambridge University Press, UK, 1998).

[49] P. Krogstrup, N. L. B. Ziino, W. Chang, S. M. Albrecht, E. Madsen M. H., Johnson, J. Nygård, C. M. Marcus, and T. S. Jespersen, arXiv:1411.6254 (unpublished).

[50] Kun Yang and Bertrand I. Halperin, Phys. Rev. B **79**, 115317 (2009).

[51] N. R. Cooper and Ady Stern, Phys. Rev. Lett. **102**, 176807 (2009).

[52] G. Gervais and Kun Yang, Phys. Rev. Lett. **105**, 086801 (2010).

[53] Chris R. Laumann, Andreas W. W. Ludwig, David A. Huse, and Simon Trebst, Phys. Rev. B **85**, 161301 (2012).

[54] W. Chickering, J. Eisenstein, L. Pfeiffer, and K. West, Phys. Rev. B **87**, 075302 (2013).

[55] Meng Cheng, Roman M. Lutchyn, Victor Galitski, and S. Das Sarma, Phys. Rev. Lett. **103**, 107001 (2009).

[56] M. Baraban, G. Zikos, N. Bonesteel, and S. H. Simon, Phys. Rev. Lett. **103**, 076801 (2009).

[57] Steven D. Bennett, Lynda Cockins, Yoichi Miyahara, Peter Grütter, and Aashish A. Clerk, Phys. Rev. Lett. **104**, 017203 (2010).

[58] Lynda Cockins, Yoichi Miyahara, Steven D. Bennett, Aashish A. Clerk, Sergei Studenikin, Philip Poole, Andrew Sachrajda, and Peter Grutter, Proceedings of the National Academy of Sciences (2010).

[59] S. Ilani, J. Martin, E. Teitelbaum, J.H. Smet, D. Mahalu, V. Umansky, and A. Yacoby, Nautre **427**, 328 (2004).

[60] Jens Martin, Shahal Ilani, Basile Verdene, Jurgen Smet, Vladimir Umansky, Diana Mahalu, Dieter Schuh, Gerhard Abstreiter, and Amir Yacoby, Science **305**, 980 (2004).

[61] Noam Sivan and Shimon Levit, Phys. Rev. B **46**, 3953 (1992).

[62] X.G. Wen, *Quantum Field Theory Of Many-body Systems: From The Origin Of Sound To An Origin Of Light And Electrons*, *Oxford Graduate Texts* (Oxford University Press, USA, 2004).

[63] M. D. Johnson and G. S. Canright, Phys. Rev. B **41**, 6870 (1990).

[64] Ady Stern, Bernd Rosenow, Roni Ilan, and Bertrand I. Halperin, Phys. Rev. B **82**, 085321 (2010).

[65] H. A. Fertig and B. I. Halperin, Phys. Rev. B **36**, 7969 (1987).

[66] John David Jackson, *Classical Electrodynamics Third Edition* (John Wiley & Sons, Inc., USA, 1998).

[67] T M Rice and M Sigrist, Journal of Physics: Condensed Matter **7**, L643 (1995).

[68] L. Fu and C.L. Kane, Phys. Rev. Lett. **100**, 096407 (2008).

[69] Grigory E Volovik and GE Volovik, *The universe in a helium droplet* (Oxford University Press, UK, 2009).

[70] M.A. Silaev and G.E. Volovik, Journal of Low Temperature Physics **161**, 460 (2010).

[71] Johan Nilsson, A. R. Akhmerov, and C. W. J. Beenakker, Phys. Rev. Lett. **101**, 120403 (2008).

[72] Masatoshi Sato and Satoshi Fujimoto, Phys. Rev. B **79**, 094504 (2009).

[73] Masatoshi Sato, Yoshiro Takahashi, and Satoshi Fujimoto, Phys. Rev. Lett. **103**, 020401 (2009).

[74] S. Das Sarma, Jay D. Sau, and Tudor D. Stanescu, Phys. Rev. B **86**, 220506 (2012).

[75] Diego Rainis, Luka Trifunovic, Jelena Klinovaja, and Daniel Loss, Phys. Rev. B **87**, 024515 (2013).

[76] D I Pikulin, J P Dahlhaus, M Wimmer, H Schomerus, and C W J Beenakker, New Journal of Physics **14**, 125011 (2012).

[77] K. Flensberg, Phys. Rev. B **82**, 180516 (2010).

[78] G. Kells, D. Meidan, and PW Brouwer, Phys. Rev. B **85**, 060507 (2012).

[79] Jie Liu, Andrew C. Potter, K. T. Law, and Patrick A. Lee, Phys. Rev. Lett. **109**, 267002 (2012).

[80] Dmitry Bagrets and Alexander Altland, Phys. Rev. Lett. **109**, 227005 (2012).

[81] Patrick Neven, Dmitry Bagrets, and Alexander Altland, New Journal of Physics **15**, 055019 (2013).

[82] Eduardo J. H. Lee, Xiaocheng Jiang, Ramón Aguado, Georgios Katsaros, Charles M. Lieber, and Silvano De Franceschi, Phys. Rev. Lett. **109**, 186802 (2012).

[83] Tudor D. Stanescu, Roman M. Lutchyn, and S. Das Sarma, Phys. Rev. B **90**, 085302 (2014).

[84] Ian Appelbaum, Applied Physics Letters **103**, (2013).

[85] Audrey Cottet, Takis Kontos, and Benoit Doucot, Phys. Rev. B **88**, 195415 (2013).

[86] Stefan Walter, Thomas L. Schmidt, Kjetil Børkje, and Björn Trauzettel, Phys. Rev. B **84**, 224510 (2011).

[87] Dong E. Liu, Phys. Rev. Lett. **111**, 207003 (2013).

[88] Chien-Hung Lin, Jay D. Sau, and S. Das Sarma, Phys. Rev. B **86**, 224511 (2012).

[89] Jason Alicea, Rep. Prog. Phys. **75**, 076501 (2012).

[90] Javier Osca, Daniel Ruiz, and Lloren ç Serra, Phys. Rev. B **89**, 245405 (2014).

[91] Tudor D. Stanescu, Sumanta Tewari, Jay D. Sau, and S. Das Sarma, Phys. Rev. Lett. **109**, 266402 (2012).

[92] Johannes Reuther, Jason Alicea, and Amir Yacoby, Phys. Rev. X **3**, 031011 (2013).

[93] Jay D. Sau and S. Das Sarma, Phys. Rev. B **88**, 064506 (2013).

[94] I. C. Fulga, F. Hassler, A. R. Akhmerov, and C. W. J. Beenakker, Phys. Rev. B **83**, 155429 (2011).

[95] M. S. Grinolds, S. Hong, P. Maletinsky, L. Luan, M. D. Lukin, R. L. Walsworth, and A. Yacoby, Nat Phys **9**, 215 (2013).

[96] D. Rugar, R. Budakian, H. J. Mamin, and B. W. Chui, Nature **430**, 329 (2004).

[97] Denis Vasyukov, Yonathan Anahory, Lior Embon, Dorri Halbertal, Jo Cuppens, Lior Neeman, Amit Finkler, Yehonathan Segev, Yuri Myasoedov, Michael L. Rappaport, Martin E. Huber, and Eli Zeldov, Nat Nano **8**, 639 (2013).

[98] H. J. Mamin, M. Kim, M. H. Sherwood, C. T. Rettner, K. Ohno, D. D. Awschalom, and D. Rugar, Science **339**, 557 (2013).

[99] L. Fu and C.L. Kane, Phys. Rev. B **79**, 161408 (2009).

[100] David Falk, Phys. Rev. **132**, 1576 (1963).

[101] A. Yacoby, S. Hart, and H. Ren, Private Communications (2014).

[102] E. A. Demler, G. B. Arnold, and M. R. Beasley, Phys. Rev. B **55**, 15174 (1997).

[103] S.M. Frolov, Ph.D. thesis, University of Illinois at Urbana-Champaign, 2005.

[104] L Weithofer and P Recher, New Journal of Physics **15**, 085008 (2013).